Results in Engineering 25 (2025) 103866

Contents lists available at ScienceDirect

Results in Engineering

journal homepage: www.sciencedirect.com/journal/results-in-engineering

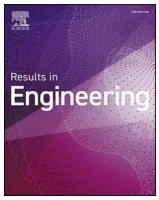

Research paper

Photodegradation of lignin biowaste catalyzed by biosynthesized zinc oxide nanoparticles using the leaf extract of *Aristotelia chilensis*

Joelis Vera [a], Wence Herrera [b], Edward Hermosilla [c,d], Heidi Schalchli [c], Ramiro Díaz [e], Paola Fincheira [c,d], Amedea B. Seabra [f], Andrés Quiroz [c,g], Gonzalo Tortella [c,d], Olga Rubilar [c,d,*]

[a] Doctoral Program in Engineering Sciences Mention Bioprocesses, Faculty of Engendering and Science, Universidad de La Frontera, Temuco, Chile
[b] Department of Chemistry and Biochemistry, University of Windsor, Windsor, Ontario, Canada
[c] Biotechnological Research Center Applied to the Environment (CIBAMA-BIOREN), Faculty of Engendering and Science, Universidad de La Frontera, Temuco, Chile
[d] Chemical Engineering Department, Faculty of Engineering and Science, Universidad de La Frontera, Temuco, Chile
[e] Department of Biological and Chemical Sciences, Faculty of Natural Resources, Universidad Católica de Temuco, Temuco, Chile
[f] Center for Natural and Human Sciences, Universidade Federal do ABC, Santo André 09210-580, Brazil
[g] Department of Chemical Sciences and Natural Resources, Faculty of Engineering and Sciences, Universidad de La Frontera, Temuco, Chile

ARTICLE INFO

Keywords:
Green synthesis
Chemical synthesis
Zinc oxide nanoparticles
Kraft lignin
Photocatalysts, photodegradation
Depolymerization

ABSTRACT

This study evaluated the photocatalytic activity of zinc oxide nanoparticles (ZnO-B) synthesized using a leaf extract of *Aristotelia chilensis* and the effect of calcination at different temperatures (400, 600, and 800 °C) on their properties and performance. The photocatalytic degradation of lignin was compared among biogenic ZnO-B, chemically synthesized ZnO (ZnO–Ch), and commercial ZnO (ZnO–C). The lignin degradation rates after 24 h were ZnO–B_400 (60.8%), ZnO–B_600 (90.57%), ZnO–B_800 (27.83%), ZnO–Ch (23.2%), and ZnO–C (80.7%). The nanoparticles were characterized by TEM, XRD, FTIR, and UV–vis spectroscopy. The physicochemical properties and photocatalytic efficiency of ZnO–B were significantly influenced by calcination temperature, with ZnO–B_600 demonstrating superior photocatalytic activity under UV-A and simulated sunlight. GC–MS analysis of lignin degradation products revealed the transformation of lignin into high-value chemicals, including 2,3-hexanediol, 1,2-benzenedicarboxylic acid diethyl ester, phthalic acid cyclobutyl isobutyl ester, 2-(1-oxo-propyl)-benzoic acid, and 4-hydroxy-2-butanone. These findings highlight the potential of biogenic ZnO-B nanoparticles in photocatalytic processes for the valorization of Kraft lignin into value-added compounds of interest to the chemical, cosmetic, and pharmaceutical industries.

1. Introduction

Lignin is a polyphenolic biopolymer that typically constitutes about 15–35% of dry weight in lignocellulosic biomass. It is predominantly found within the cell wall of plants, thereby providing rigidity, imperviousness, and resistance to biodegradation to the plants [1]. Lignin is obtained as a by-product during the chemical pulping of wood, the primary industrial method used to separate lignin from cellulosic fibers for the production of paper and related products [2,3]. In Chile, the Kraft pulping process, widely used by the paper industry, generates substantial amounts of lignin, with only a small fraction commercially utilized (2 wt%), while the remainder is burned for energy, contributing to resource wastage and environmental issues [4–9]. Therefore, the development of cost-effective and sustainable technologies for lignin valorization is crucial to advancing the circular economy [8,10,11]. The structural complexity and heterogeneity of lignin make its valorization challenging, yet several depolymerization technologies have emerged, converting lignin into low-molecular-weight aromatic molecules suitable for integration into the chemical industry [6,12]. Various technologies for lignin conversion have emerged to date, including thermochemical processes (e.g., pyrolysis and microwave-assisted methods), physical methods (e.g., ball milling, ultrasonication, and plasma irradiation), biological approaches (using fungi, bacteria, and enzymes), and chemical catalysis processes (catalyzed by acids, bases, metals, and assisted by ionic liquids, supercritical fluids, and oxidizing agents) [2,13–15]. Although existing methods have demonstrated high efficiency in lignin depolymerization, many of these technologies present significant drawbacks. These include: i) the severity of reaction

* Corresponding author.
E-mail address: olga.rubilar@ufrontera.cl (O. Rubilar).

https://doi.org/10.1016/j.rineng.2024.103866
Received 10 September 2024; Received in revised form 19 December 2024; Accepted 28 December 2024
Available online 30 December 2024

conditions, such as extreme pH, high temperatures (250–800 °C), and pressures (5–10 MPa), which significantly increase energy consumption and raise capital and maintenance costs; ii) the use of relatively expensive catalysts (e.g., Pd, Pt, Rh, and Ru); and iii) the production of highly corrosive effluents [2,15], which involves additional costs due to the need for further treatment to mitigate the generated by-products. While biological methods are more cost-effective in terms of raw materials, their considerably longer processing times limit their industrial applicability. In this scenario, heterogeneous photocatalytic processes constitute an attractive alternative to conventional methods, as they can significantly reduce overall process costs and environmental impact due to their low energy consumption and secondary–pollution–free operation. This method uses electromagnetic radiation (within the UV and visible range) and a semiconductor under mild conditions (25 °C and 0.9869 atm) to generate radical species that are highly reactive, minimally selective, and short-lived, with the ability to decompose a wide range of recalcitrant chemicals as well as inactivate microorganisms [16,17].

Zinc oxide (ZnO), a semiconductor with a bandgap of 3.37 eV, has been extensively used as a photocatalyst for organic pollutant degradation due to its photochemical stability, nontoxicity, ease of synthesis, and high efficiency [18–20]. Although ZnO has shown good activity for lignin photodegradation in aqueous media, previous studies often focus on overall degradation efficiency without identifying specific products derived from these treatments [21–24]. Furthermore, the reliance on chemically synthesized ZnO nanoparticles (ZnO–NPs) reduces the sustainability of photocatalytic processes due to the use of hazardous reagents such as solvents, surfactants, and reducing agents [25,26]. Biogenic synthesis of nanoparticles using plant extracts represents a greener alternative, leveraging the phytochemical richness of plants to serve as reducing and stabilizing agents [27–33]. Typically, an aqueous solution of the metal precursor is continuously mixed with aqueous plant extracts. The reaction is rapid (lasting only a few minutes) and is conducted at temperatures ranging from 25 to 100 °C under ambient pressure. This method offers a high degree of precision and control over the characteristics of the nanoparticles, such as size, morphology, and crystal phase, by adjusting synthesis conditions, including pH, reaction temperature, plant species, plant parts used, and plant extract concentrations [34,35]. This approach allows for the optimization of the material's physicochemical properties, tailoring it for specific applications.

While various plant species have been used to prepare ZnO–NPs [36–38], this study utilizes *Aristotelia chilensis* (maqui), a native Chilean shrub known for its antioxidant-rich leaf extracts and medicinal applications for the synthesis of ZnO–NPs [39,40]. In a previous study, we reported that leaf extract from *A. chilensis* was more effective at synthesizing ZnO–NPs compared to extracts from *Galega officinalis, Buddleja globosa*, and *Eucalyptus globulus*. This increased effectiveness was closely associated with the higher antioxidant activity of the *A. chilensis* leaf extract [41]. *A. chilensis* leaves are rich in phytochemicals, including phenolic acids (54.36%), flavonoids (42.10%), non-iridoid monoterpene indole alkaloids, tannins, and lipophilic compounds. Key phenolic compounds, such as galloyl and caffeoyl quinic acids, provide antioxidant activity, while flavonoids like quercetin and kaempferol offer anti-inflammatory benefits and may aid in diabetes management. Alkaloids suggest potential neuropharmacological effects, tannins contribute to antibacterial properties, and lipophilic compounds like α-tocopherol (vitamin E) and β-sitosterol support antioxidant activity and may help lower cholesterol levels. [41–43].

Typically, the photocatalytic activity of biogenic ZnO–NPs (ZnO–B) has been assessed using synthetic dyes or other low molecular weight contaminants [44–46]. However, this study evaluates for the first time, the photocatalytic activity of ZnO–B for lignin degradation. The effects of calcination temperature on the physicochemical properties and photocatalytic activity of ZnO–B were thoroughly investigated, focusing on key process parameters such as pH, light sources, and mixing conditions. For comparative purposes, chemically synthesized ZnO–NPs (ZnO–Ch) and commercially available ZnO–NPs (ZnO–C) were used as reference materials. Furthermore, the lignin degradation products generated by ZnO–B were identified through GC–MS analysis to evaluate the feasibility of the process in generating value-added chemicals.

2. Materials and methods

2.1. Green synthesis of ZnO–NPs using leaf extract from A. chilensis

ZnO–NPs were prepared using aqueous leaf extract from *A. chilensis* according to our previous work [40]. Initially, the leaf extract was prepared by mixing 10 g of cleaned and dried leaves with 200 mL of distilled water in a beaker, which was then heated at 60 °C for 1 h. The extract was filtered through Whatman No. 1 filter paper (Whatman, USA). Subsequently, 60 mL of the extract was combined with 20 mL of 0.05 M zinc acetate dihydrate (CAS: 5970-45-6, Sigma-Aldrich, USA) under magnetic stirring and heated at 60 °C for 1 h. The resulting precipitate was separated from the reaction solution by centrifugation at 12,000 rpm for 10 min, then washed several times with distilled water until the pH of the suspension reached approximately 6–7. The precipitate was then dried in an oven at 80 °C. Following findings from previous research, the solid product was transferred to a ceramic crucible and calcined at 400, 600, and 800 °C for 3 h. The samples were then stored for further use. The nanoparticle samples were labeled as ZnO–B_400, ZnO–B_600, and ZnO–B_800, corresponding to the calcination temperatures.

2.2. Chemical synthesis of ZnO–NPs

ZnO–Ch NPs were synthesized using conventional chemical methods following Koutu et al. (2016) [47]. In this process, 50 mL of zinc acetate dihydrate (0.1 M) was slowly added dropwise to 50 ml of sodium hydroxide solution (0.1 M; CAS: 1310-73-2) and maintained under constant stirring at 90 °C for 2 h using a reflux system. The reaction resulted in the formation of a white precipitate, which was washed multiple times with water until the pH reached approximately 6–7. The obtained precipitate was transferred to a ceramic crucible, dried overnight at 80 °C, calcined at 400 °C for 2 h, and stored for further use. For comparison, ZnO—NPs (CAS:1314-13-2) were purchased from Merck, USA. These commercial nanoparticles (ZnO—C), with an average particle size of 50 nm, were used as received.

2.3. Characterization of ZnO–NPs

The characterization of the samples was performed using several analytical instruments. Dynamic light scattering (DLS) analysis was conducted using a Malvern Zetasizer Nano ZS90 (Malvern Instruments, Inc., UK) to determine the hydrodynamic diameter (Z-average), surface charge (zeta potential), and polydispersity index (PDI). The optical properties of the samples were assessed using a Thermo Scientific Evolution™ 60S UV–Vis Spectrophotometer (Thermo Fisher Scientific, USA). Fourier-transform infrared spectroscopy (FTIR) was employed to confirm the involvement of phenolic compounds in biogenic nanoparticle formation and to assess the purity of the synthesized nanoparticles. For FTIR analysis, the powder samples were placed on the ATR crystal of a Cary 630 FTIR Spectrometer (Agilent Technologies, USA), with spectra collected in the range of 400–4000 cm−1. The crystalline structure and composition of the nanoparticles were analyzed using a Rigaku SmartLab X-ray Diffractometer (Rigaku Corporation, Japan), equipped with a Bragg-Brentano (theta/theta) goniometer and a D/teX Ultra 250 solid-state detector. XRD patterns were obtained using Cu-Kα radiation (λ = 1.5406 Å) at 30 kV and 40 mA, in the 2Theta range of 3–60°, with a step size of 0.01° and a scan rate of 0.5°/s. The morphology and particle size distribution of the nanoparticles were determined using a Carl Zeiss LIBRA® 120 PLUS Transmission Electron Microscope (TEM) (Carl Zeiss AG, Germany). Approximately 100

nanoparticles were measured in random fields of the TEM images to estimate the average particle size and size distribution.

2.4. Assays of photocatalytic Kraft lignin degradation

Photocatalytic assays were carried out using a 500 mL quartz beaker in a chamber equipped with three UVA lamps (Philips, 40 W) placed at a distance of 30 cm between the lamp crown and the irradiation object (Fig. 1). For each run, 100 mL of a 0.1 g/L Kraft lignin solution (CAS: 8068-05-1) prepared in 0.05 M sodium hydroxide was added to the reaction vessel along with the desired amount of catalyst. The resultant suspension, with a natural pH value of 13, was magnetically stirred at 500 rpm for 1 h at 25 °C in dark conditions to establish the adsorption-desorption equilibrium between the photocatalyst surface and lignin molecules [48,49]. Subsequently, the suspension was exposed to light for 24 h under continuous magnetic stirring. The effect of pH on the photocatalytic activity of ZnO—NPs for lignin degradation was then evaluated by adjusting the reaction medium to pH values of 5, 7, 9, and 13, representing acidic, neutral, and basic conditions. Photocatalytic assays were also performed under simulated sunlight irradiation using a 300 W Osram Ultra–Vitalux lamp. The emission spectra of both the simulated sunlight and UVA lamps are shown in Figure S1.

The photodegradation of Kraft lignin was monitored by collecting 1 mL aliquots from the reaction mixture every 4 h. These aliquots were centrifuged at 15,000 rpm for 10 min to remove the ZnO nanoparticles. The absorbance of the resulting supernatants was measured at 290 nm using a Thermo Scientific Evolution™ 60S UV–Vis Spectrophotometer (Thermo Fisher Scientific, USA). The lignin concentration in the supernatants was determined using a previously established calibration curve. Finally, the photocatalytic activity of the nanomaterials was quantified by calculating the percentage of remaining lignin concentration at specific time intervals relative to the initial lignin concentration, using the following expression [50]:

$$\text{Lignin degradation } (\%) = \left[\frac{(C_0 - C_t)}{C_0}\right] \times 100 \quad (1)$$

where C_o represents the initial lignin concentration and C_t is the lignin concentration at a specific reaction time.

The kinetic efficiency was evaluated by determining the rate constant (k) and half-life time ($t_{1/2}$). The data obtained for the photodegradation of Kraft lignin were adjusted to pseudo-first–order expressed by the following equation:

$$\text{Ln}\left(\frac{C_t}{C_0}\right) = -kt \quad (2)$$

k was calculated from the slope of the linear plots of ln (C_t/C_0) vs irradiation time. The $t_{1/2}$ was determined according to Eq. (3) for the pseudo–first-order kinetics.

$$t_{1/2} = \frac{\text{Ln } 2}{k} \quad (3)$$

2.5. Recovery and recycling of nanoparticles

The reusability of the nanomaterials was assessed through multiple cycles. After each experiment, the reaction solution was centrifuged to separate the nanocatalyst. The recovered nanocatalyst was washed several times with deionized water, air-dried at 70 °C for 1 h, and subsequently reused in the following photocatalytic degradation assays. This procedure was repeated for five consecutive reaction cycles, with all cycles conducted under the same conditions outlined in Section 2.4.

2.6. Determination of produced $^{\bullet}OH$ radicals during the photocatalytic process

Formation of malondialdehyde (MDA) via oxidation of 2–deoxyribose (2–DR) by hydroxyl radicals was used to confirm the *insitu* radicals generation ($^{\bullet}OH$) in the reaction medium (Eq. (4)) [51–53]. The concentration of MDA was calculated with a thiobarbituric acid (TBA) reaction forming a pink compound (Eq. (5)). Briefly, in a screw-capped glass tube 500 µL of the sample (taken at different time intervals) and 50 µL of 28 mM 2–DR were added. The reaction was carried out for 1 h at 37 °C and stopped by adding 500 µL 2.8% w/v trichloroacetic acid (TCA) and 500 µL of 1% w/v TBA in 50 mM of NaOH. After boiling the sample in a water–bath for 20 min at 90 °C, the solution was cooled to 25 °C. Finally, a spectrophotometer was utilized to measure the absorbance at 532 nm. Blanks containing water instead of 2–DR were used to correct the final absorption values. The reaction products were expressed in nmol/mL using the molar extinction coefficient ($\varepsilon = 1.36 \times 10^5\ M^{-1}cm^{-1}$) [54].

$$^{\bullet}OH + \text{2–Deoxyribose} \rightarrow \text{MDA} \quad (4)$$

$$\text{2–TBA} + \text{MDA} \rightarrow \text{chromogen} \quad (5)$$

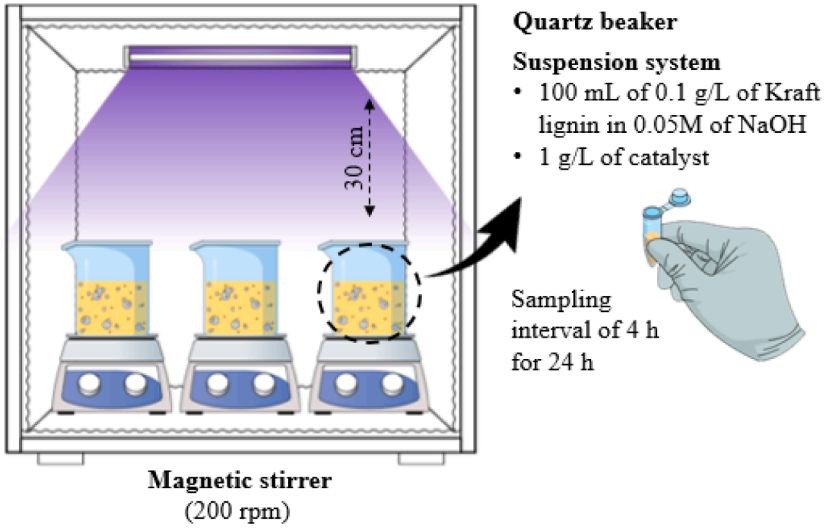

Fig. 1. Reaction system for the photocatalytic degradation tests.

2.7. Identification of the lignin degradation products

The lignin depolymerization process produces various products: gas, solid residues, and bio-oil. This bio-oil is grouped as water-soluble organic (WSO) and heavy bio-oil [55,56]. Fig. 2 displays the product separation technique schematic representation. This occurs as follows: first, after each photocatalytic trial, the nanocatalyst was removed from the solution through centrifugation at 15,000 RPM x 10 min. Then, the remaining lignin was precipitated by acidification with 37% HCl (pH of ~1.5−2) and separated by filtration using a 0.22 μm membrane. The liquid phase containing water-soluble organics was subjected to a liquid-liquid extraction using ethyl acetate as an organic solvent, which was completely removed in a rotary evaporator set at 40 °C.

The composition of the degradation products at various reaction times (4, 8, 12, 16, 20, and 24 h) was analyzed using Gas Chromatography-Mass Spectrometry (GC–MS) on a Shimadzu GCMS-QP2010 system (Shimadzu Corporation, Japan), which was coupled with a Mass Spectrometric Detector (MSD) and a Flame Ionization Detector (FID). The analyses were performed using an HP-5MS capillary column (30 m × 0.25 mm × 0.25 μm, Agilent Technologies, USA) for separation. MSD and FID detectors were utilized for compound identification and quantification respectively. The components were identified by comparing their retention indices and mass spectra with the NIST 08 and NIST 08s (Stein, 2008) library or literature data [57–59].

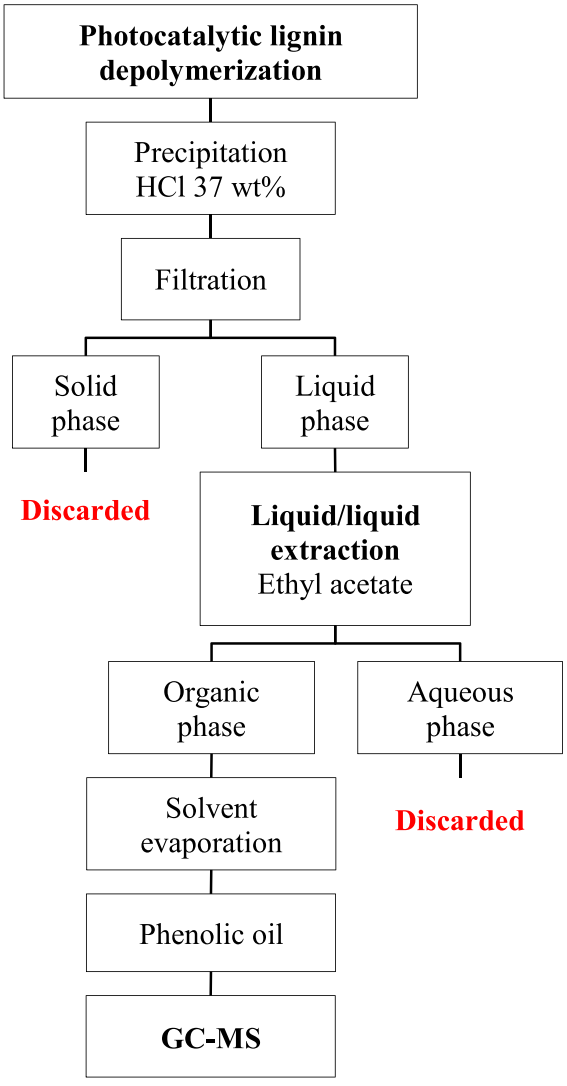

Fig. 2. Scheme of the product separation process following the photocatalytic treatment of lignin.

3. Results and discussion

3.1. Characterization of ZnO–NPs

3.1.1. UV–visible spectroscopy

The synthesis of ZnO nanoparticles (ZnO–NPs) using *A. chilensis* leaf extracts was successfully achieved, as evidenced by the UV–visible spectroscopy results. The absorption peaks of the biologically synthesized samples at various calcination temperatures (ZnO–B_400, ZnO–B_600, ZnO–B_800) were observed at 364, 369, and 375 nm, respectively, while ZnO–C and ZnO–Ch showed peaks at 357 nm (Fig. 3A), consistent with the characteristic band of hexagonal ZnO. These results indicate that the leaf extract-mediated synthesis produced nanoparticles with the expected optical properties. The observed blue shift in the UV absorption spectra for ZnO–B_400, ZnO–B_600, and ZnO–C, compared to ZnO–B_800 and ZnO–Ch, suggests smaller particle sizes, which were influenced by the calcination temperature of ZnO-B. Biogenic ZnO nanoparticles synthesized using extracts of *Cayratia pedata* and zinc nitrate as the precursor salt exhibited an absorption peak at 320 nm [60]. Similarly, ZnO nanoparticles synthesized with *Momordica charantia* leaf extract displayed an absorption maximum at 374 nm [61], which could suggest that specific phytochemicals in plant extracts can influence the optical properties of the synthesized nanoparticles.

Given the importance of ZnO in optoelectronic applications [62], its band gap (Eg) was estimated using the equation Eg (eV) = 1240/λ (nm), where λ is the wavelength of the maximum peak of UV–vis absorption spectra. The Eg values obtained were 3.40, 3.36, 3.31, 3.28, and 3.47 eV for ZnO–B_400, ZnO–B_600, ZnO–B_800, ZnO–Ch and ZnO–C, respectively. An increase in calcination temperature reduced the Eg values as theoretically calculated. This shift can move the absorption edge of ZnO into the visible range, thereby enhancing the visible light photocatalytic activities of ZnO [63,64].

3.1.2. XRD analysis

The XRD patterns of the ZnO samples are presented in Fig. 3B. It can be seen that all patterns exhibited five well–defined diffraction reflections at 2 theta values of 31.7°, 34.1°, 36.1°, 47.6° and 56.5° which correspond to the (100), (002), (101), (102) and (110) planes of wurtzite hexagonal phase ZnO, according to the standard PDF database (JCPDS No. 36–1451). The XRD pattern of biogenic samples showed background noise due to the presence of organic matter from plant extract used for its synthesis. The lower intensity and the broad base of diffraction peaks of the ZnO–B samples reflect that the synthesized materials had smaller crystallite sizes compared to ZnO–Ch and ZnO–C. The XRD pattern of ZnO–B samples showed increased intensity and sharpness of peaks with increased calcination temperature, suggesting that the degree of crystallinity and crystallite size of the ZnO phase increases.

The crystallite sizes of the prepared materials were estimated from the XRD data using both the Debye–Scherrer equation and Williamson–Hall plot (W–H plot). The equations used for these purposes are described in our previous work [40]. The calculated crystallite size values are presented in Table 1. Green–prepared particles at 400 and 600 °C showed the lowest crystallite sizes, whereas the highest were for ZnO–Ch, ZnO–B_800, and ZnO–C. The lower values for ZnO–B_400 and ZnO–B_600 can be attributed to the effective role of polyphenolic constituents of the plant extract acting as capping and stabilizing agents during synthesis [40]. However, at a calcination temperature of 800 °C, the thermal decomposition of a large part of the organic matter increases the crystal growth rate, resulting in larger crystallites.

The lattice strain (ε), so-called microstrain, was determined from the slope of the linear section of the W–H plot. As can be seen in Table 1 ε values decreased with increasing crystallite size. The larger ε, the greater the lattice heterogeneity [65,66]. Therefore, in the biological synthesis of ZnO—NPs by *A. chilensis* the phytochemical species limits particle

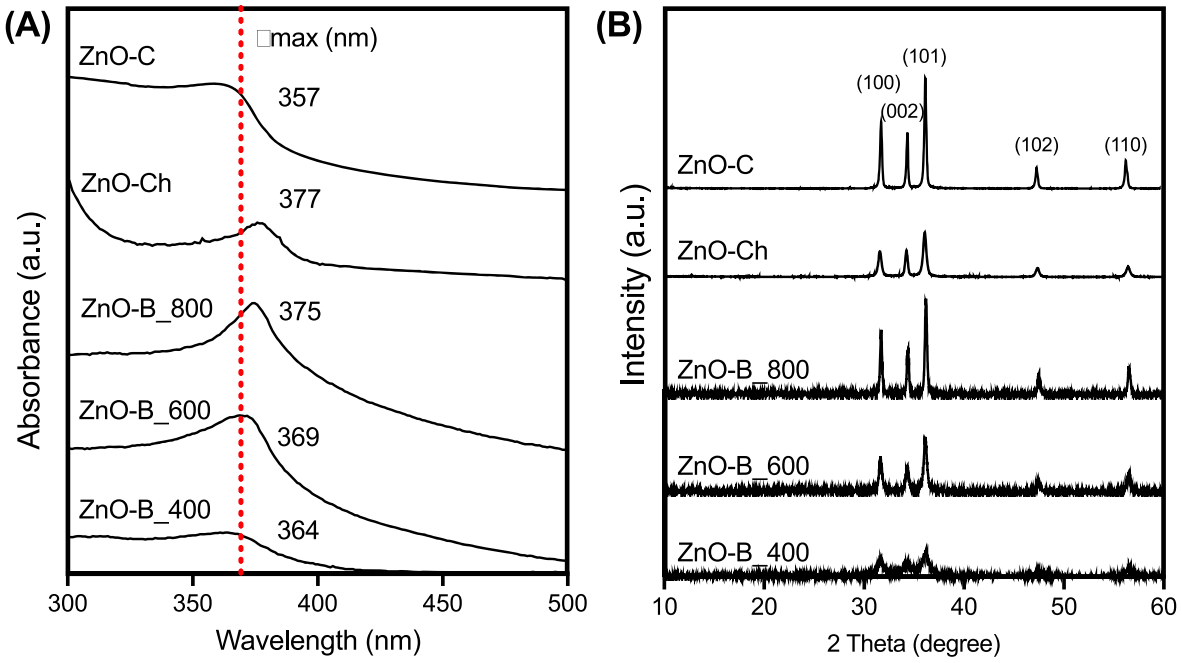

Fig. 3. (A) UV–visible spectra and (B) XRD patterns of ZnO–NPs.

Table 1
Crystallite size estimated by Debye–Scherrer and Williamson–Hall.

Samples	Crystallite size (nm)		$\varepsilon x10^{-3}$
	Scherrer equation	W–H plots	
ZnO–C	31.73	46.20	1.0
ZnO–Ch	22.76	29.49	0.7
ZnO–B_800	31.84	40.76	0.9
ZnO–B_600	18.84	18.24	7.6
ZnO–B_400	7.89	4.50	6.9

growth and crystallization, and induces atomic and structural disorder. These characteristics could affect the reactivity of ZnO—NPs by controlling factors such as crystal orientation, crystal facet exposure, and atom rearrangement [67–69].

3.1.3. FTIR analysis

Fig. 4 presents the FTIR spectra measured from 400 to 4000 cm^{-1} for prepared (chemical and green) and commercial samples. This technique was used to assess the chemical compositions and purity of the materials studied. All spectra exhibit a broad absorption band at around 3400 cm^{-1} and a minor band at approximately 1620 cm^{-1}, which correspond to the stretching and bending vibration of O–H bonds from water molecules adsorbed on the surface of ZnO–NPs. The strongest band, observed between 400 and 500 cm^{-1}, is attributed to the stretching mode of the Zn–O bond, thus confirming the presence of ZnO. The displacement and appearance of these absorption bands depend on the morphology of ZnO [70,71]. ZnO–Ch exhibited absorption peaks at 1038, 1383, and 1507cm^{-1} attributed to C–O stretching and, symmetric and asymmetric O–C–O stretching modes, respectively, which can be assigned to traces of the precursor salt that remained unreacted during the synthesis process. On the other hand, no organic groups were detected in the commercial sample (ZnO–C), confirming its high purity. The absorption bands detected at 1480, 1420, and 1048 cm^{-1} for ZnO–B samples are attributed to the stretching vibration of C═C, C–N, and C–O [72–74] which confirm the presence of bioactive compounds from plant extract on the particles after calcination. As shown in Fig. 4, the intensity of these bands decreases gradually with the calcination temperature increases due to the thermal decomposition of organic compounds. This fact was also reflected in the physical appearance of the samples obtained, the higher the calcination temperature, the lighter the powder color.

3.1.4. DLS analysis

Z–average, PDI, and zeta–potential of ZnO–NPs suspended in distilled water were determinate (Table 2). Z–average of ZnO–NPs provides crucial information on how these particles will behave in aqueous dispersion media. ZnO–C and ZnO–Ch exhibited Z–average values of 204.80 and 556.40 nm respectively, while the samples produced by green synthesis exhibited Z–Average ranging from 1108.67 to 535.87 nm. At lower calcination temperatures samples prepared using the biological method showed the highest values, probably due to particle coarsening caused by residual amorphous carbon on the ZnO due to incomplete combustion of plant extract. As the calcination temperature increases, the quantity of organic compounds decreases, resulting in a reduction in the Z–average value.

The high Z–average values experimentally found in this work suggest that the samples studied have a high agglomeration tendency in the water, considering the bias of DLS to larger sizes [75,76]. During a DLS measurement, large particles or even aggregates of the smaller particles can mask the results, resulting in Z–average values that are not quantitatively informative. However, we have provided this data for comparison with existing literature, as DLS remains a commonly used and preferred technique for characterizing nanoparticles dispersed in a simple solvent or biological environment.

PDI values obtained for all ZnO samples ranged from 0.1 to 0.4. A value higher than 0.5 suggests a very broad size distribution of particles in the sample [77–79]. In this sense, PDI values in Table 3 revealed that the size distributions of all samples are monodispersed.

The zeta–potential is a measure of the surface charge and stability of particle dispersions, which can determine the interactions between the catalyst surface and substrate. The average Rzeta–potential values of ZnO–C and ZnO–Ch were positive. By contrast, ZnO–B samples showed negative zeta–potential due to the presence of a capping layer formed around of particle by negatively charged functional groups from the *A. chilensis* aqueous extract. Zeta–potential values exceeding +30 mV or falling below −30 mV indicate a strong repulsive force between particles, enhancing dispersion stability [80]. Therefore, zeta–potential

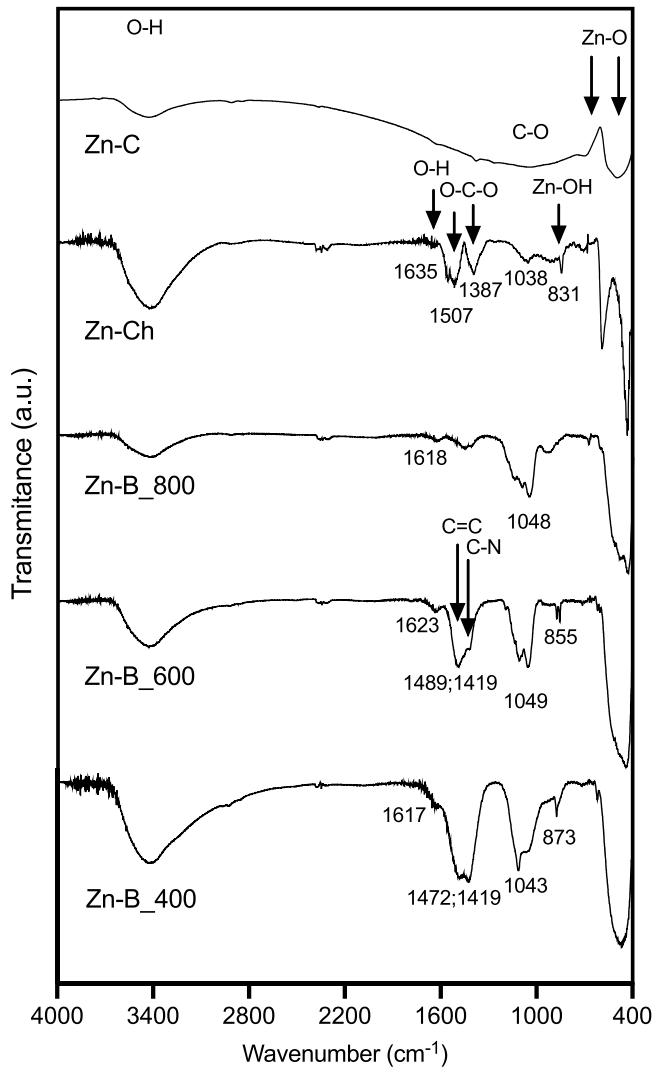

Fig. 4. FTIR spectra of ZnO—NPs.

Table 2
Physical characterization of ZnO–NPs.

Samples	Z–average (nm)	PDI	Zeta–potential (mV)
ZnO—C	204.80 ± 6.87	0.40 ± 0.02	40.73 ± 1.10
ZnO—Ch	556.40 ± 5.01	0.17 ± 0.04	27.97 ± 0.31
ZnO–B_800	535.87 ± 3.39	0.20 ± 0.02	−11.03 ± 0.30
ZnO–B_600	771.50 ± 5.83	0.15 ± 0.04	−10.08 ± 0.76
ZnO–B_400	1108.67 ± 7.77	0.34 ± 0.06	−14.93 ± 0.06

The results are expressed as mean±standard deviation.

values of ZnO–C, and ZnO–Ch suggest a good dispersity and stability of the ZnO particles. At the same time, the results of samples synthesized via green routes confirm that the obtained ZnO particles have lesser stability. Hence, the particle exhibits an aggregation propensity.

3.1.5. TEM analysis

The TEM images of samples studied in this work are shown in Fig. 5. From the images, it is observed that all the powders had predominantly spherical morphology. Some particles with hexagonal shapes were also evident. In the particular case of ZnO–C, particles with a rod-like morphology were present. Through the size distribution histograms fitted by a lognormal function, it was found that the mean diameter of particles (D) was 13.0 ± 6.1, 27.5 ± 26.5, 69.8 ± 120.6, 99.0 ± 1171.9 and 29.6 ± 903.0 nm for ZnO–B_400, ZnO–B_600, ZnO–B_800, ZnO–Ch and ZnO–C, respectively (Fig. 6). ZnO–Ch and ZnO–C were characterized by exhibiting the highest standard deviation or greater particle size heterogeneity. On the other hand, an increase in the calcination temperature during the synthesis of ZnO–B resulted in larger particle size and higher standard deviation, which led to a reduction in the superficial area and increased particle size heterogeneity. It has been reported that calcination temperature significantly influences the size and morphology of ZnO nanoparticles. Studies have demonstrated that higher temperatures generally result in larger particle sizes, primarily due to increased agglomeration [24,60,81]. Therefore, it is expected that these factors could influence the catalytic activity.

3.2. Photocatalytic activity of Kraft lignin degradation ZnO–B NPs

3.2.1. Effect of calcination temperature

The assays photocatalytic performance of ZnO–B was assessed by measuring the photodegradation of Kraft lignin at natural pH 13 under UVA radiation at different time intervals. An adsorption-desorption equilibrium period in darkness conditions for 1 h was established (Fig. 6). No degradation of Kraft lignin was observed in the photolysis assay in the catalyst absence. The ZnO–B_600 catalyst demonstrated the highest lignin degradation, reaching 91%, followed by ZnO–B_400 at 60.7% and ZnO–B_800 at 28.0%. In contrast, the reference samples, ZnO–Ch and ZnO–C, achieved lignin degradation rates of 23.2% and 80.7%, respectively. The effect of the calcination temperature on the photocatalytic activity of ZnO for lignin degradation was closely related to its physicochemical properties. As the calcination temperature increased, the particle size of ZnO increased while the surface area decreased, leading to decreased lignin degradation. The lower lignin degradation observed for ZnO–NPs calcined at 400 °C, compared to those calcined at 600 °C, can be attributed to the higher content of residual organic compounds on the ZnO–B_400 surface. These residuals may obstruct and reduce the availability of active sites for interaction with lignin molecules, thereby decreasing the photocatalytic activity. Recently, Sedefoglu (2024) investigated the effect of calcination temperature (400 °C, 600 °C, and 800 °C) on ZnO nanoparticles synthesized using *Myrtus communis* extract for methylene blue degradation. The study reported that while increasing the calcination temperature led to a reduction in particle size, it negatively impacted the photocatalytic performance of the ZnO [44].

This work presents, for the first time, the potential of ZnO biogenic nanoparticles for lignin degradation. In comparison, studies on chemically synthesized ZnO nanoparticles report varied results. Lenka et al. (2023) demonstrated that ZnO nanosheets (1 g/L) achieved 93% lignin degradation within 2 h at pH 9. They attributed this high performance to the nanosheet morphology of ZnO, which may enhance the generation and stabilization of •OH radicals [24]. In another study, Mazarji et al. (2019) showed that ZnO supported on graphene oxide (1.2 g/L) achieved a maximum of 52% degradation of Kraft lignin in 240 min under UV light. They used potassium iodide as a sacrificial electron donor, which reacted irreversibly with the photogenerated valence band holes, thereby controlling the generation of •OH radicals [22]. Although our results were obtained over a much longer period (24 h), they demonstrate comparable or even superior lignin degradation, showcasing the potential of biogenic ZnO NPs for lignin degradation over extended durations. Moreover, the performance of ZnO NPs can vary significantly depending on the configuration of the photocatalysis assays. Key factors influencing performance include the intensity and distribution of light, the homogenization of the solution, and the specific reactor setup. Therefore, the photocatalytic activity for lignin degradation of biogenic nanoparticles (ZnO–B_600) was compared with that of chemically synthesized and commercial ZnO–NPs counterparts under the same photocatalytic conditions. As can be seen, higher lignin degradation was obtained when ZnO–B_600 was used (Fig. 6). The ZnO–C exhibited lignin degradation up to 81 %, while ZnO–Ch was less effective, showing 23% of Kraft lignin degradation. These results could be attributed to the

Table 3
Photocatalytic degradation of lignin by ZnO–NPs reported.

Catalyst	Catalyst synthesis	Substrate	Reaction conditions	Lignin degradation	Main products	Ref
ZnO (1 g/L)	Commercial from Merck	Lignin from wheat straw (0.1 g/L)	NaOCl/ UVA/ 5h/ 25 °C/ pH=11	84%	–	[21]
ZnO (0.5 g/L)	Commercial	Sodium salt of lignosulfonate (0.1 g/L)	Visible/ 4h/ 25 °C	–	–	[88]
ZnO (0.05 g/L)	Chemical	Kraft lignin (0.1 g/L)	KI/ UV/4h/25 °C	62%	–	[22]
ZnO (0.1 g/L)	Commercial from SCRC	Sodium of lignosulfonate (0.1 g/L)	UV/ 1h/ 25 °C/ pH=7.4	60%	–	[23]
ZnO (0.6 g/L)	Chemical	Synthetic lignin (0.04 g/L)	UVB/ 70 min/ 25 °C/ pH=8	30%	–	[89]
ZnO (1 g/L)	Chemical	Alkaline lignin (0.1 g/L)	Visible/ 2h/ 25 °C/ pH=9	93%	–	[24]
ZnO/Bi (0,1 g)	Chemical	Organosolv lignin (0,1 g/L)	UV/ 1h/ 25 °C	97%	Phenols (21,6%), creosol (16%), veratrole (12%)	[90]
ZnO@AgCl–Ag (0,5 g/L)	Chemical	Kraft lignin (0,025 g/L)	Solar light/ 1h/ 25 °C	100%	Vanillin and syringaldehyde	[49]
ZnO (1 g/L)	Biological	Kraft lignin (0,1 g/L)	UVA/ 24 h/ 25 °C/ pH=13	91%	See Table 4	This work

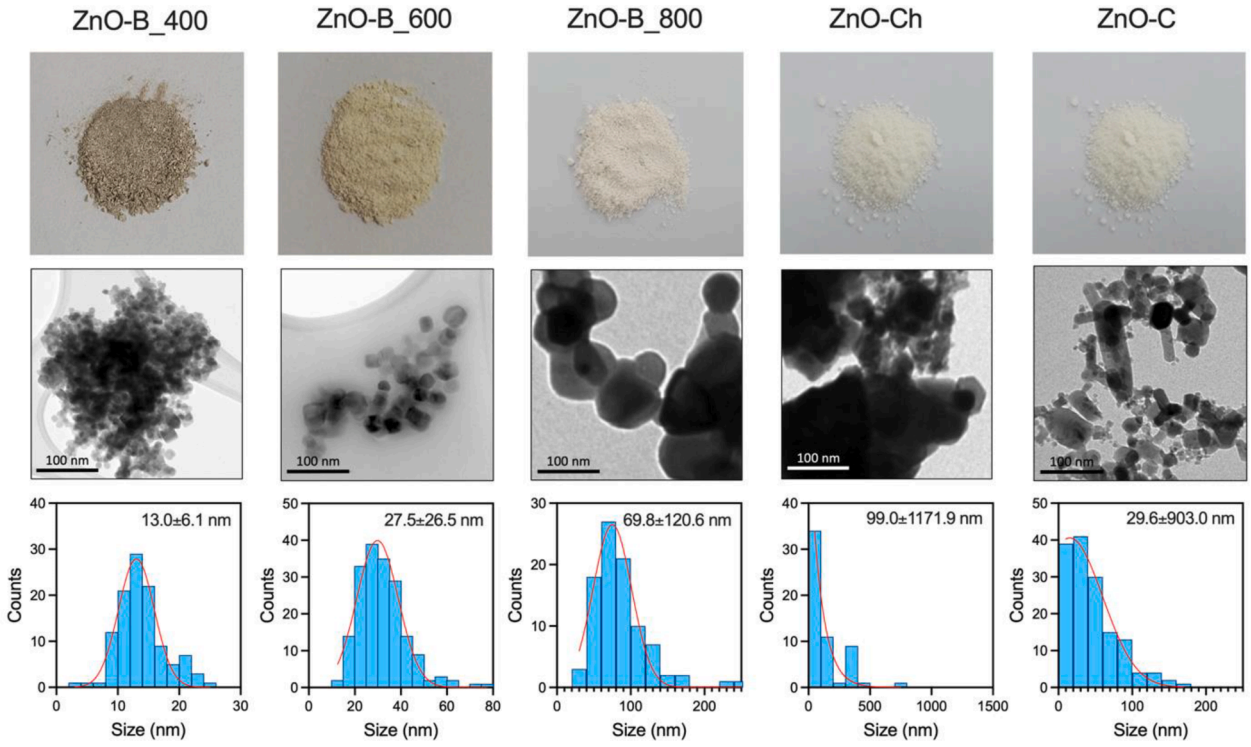

Fig. 5. Macroscopic appearance of nanopowders, TEM images, and particle size distribution histograms for ZnO–B_400, ZnO–B_600, ZnO–B_800, ZnO–Ch, and ZnO–C.

physicochemical characteristics of ZnO–B_600. The homogeneous distribution and smaller particle size, indicating a greater number of active sites, along with the highest lattice strain (as presented in Table 2), resulting in the highest surface energy, collectively contributed to enhancing its effectiveness. The results suggest that biogenic nanoparticles represent an excellent alternative to commercial ZnO–NPs.

3.2.2. *Effect of the light source and homogenization method*

The influence of physical parameters such as light source (UVA and visible) and mixture homogenization method (magnetic stirring and orbital rotation) on the photocatalytic activity of ZnO–B_600 was also evaluated. The photocatalytic degradation of lignin by ZnO–B_600 was 18% higher using magnetic stirring than orbital shaking (Fig. 7A). Thus, the implementation of magnetic stirring contributed to more efficient homogenization of the mixture between the catalyst and Kraft lignin solution for photocatalytic degradation. Besides, efficient homogenization increases the mass transfer and the probability of contact between the free hydroxyl radicals (•OH) generated and the substrate.

The photocatalytic performance of ZnO–B_600 under UVA and simulated sunlight sources was also studied (Fig. 7A). No significant difference was observed in the lignin degradation values obtained using simulated sunlight and UVA radiation. Similar results were obtained when the reaction mixture was exposed to natural mid-day summer sunlight, on a clear day. This phenomenon can be attributed to the capability of ZnO–NPs to absorb a broad light spectrum, extending into the UV–visible region. UV radiation is part of the spectrum of

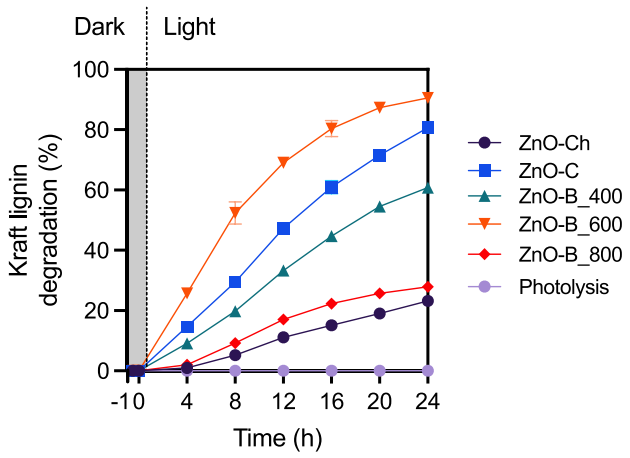

Fig. 6. Photocatalytic degradation (%) of Kraft lignin solution (0.1 g/L) catalyzed by ZnO–NPs samples (1 g/L).

electromagnetic radiation emitted by the sunlight lamp used and includes the wavelength range from 280 to 400 nm: UVB (280–315 nm) and UVA (315–400 nm). UVB rays have higher energy levels than UVA rays, which typically can enhance the photocatalytic performance of semiconductors. In this sense, sunlight utilization as a cost-effective energy source can contribute to the feasibility of photocatalytic technologies.

3.2.3. *Effect of pH*

The effect of the initial pH of the reaction medium on the photocatalytic activity of ZnO−B_600 was evaluated over a pH range of 5 to 13. As shown in Fig. 7B, the highest lignin degradation was achieved at pH 13, reaching 91%. At lower pH values, lignin degradation ranged from 34.1% to 37.7% after 24 h of reaction. This aligns with previous findings that lignin degradation through photocatalytic processes is more efficient under basic conditions (pH ≥ 9) [21,22]. It is known that pH can alter the surface charge stability of ZnO, particle interactions, and the equilibrium structure of Kraft lignin [82,83]. The zeta potential analysis for ZnO–B_600 and Kraft lignin was conducted across a range of pH values to assess their surface charge behavior (Fig. 7C). It can be observed that Kraft lignin and ZnO–B_600 exhibit very similar zeta potential values at pH 5, 7, and 9. At pH 13, Kraft lignin exhibits a slightly lower zeta potential compared to ZnO–B_600. Additionally, as the pH increases, the surface of ZnO becomes progressively more negatively charged, attributed to the adsorption of OH^- ions (Fig. 7C). The presence of large amounts of OH^- ions on the ZnO surfaces as well as in the reaction medium promotes the generation of •OH radical [84], which promotes the removal of protons from phenolic units of lignin, enhancing the efficiency of its degradation. Conversely, at acidic pH, the abundance of protons suppresses the formation of phenoxide species, reducing the efficiency of phenoxide ion generation [24] With increasing pH, the electrostatic repulsion between the lignin anions and the ZnO surface also increases, hindering interaction. As a result, the diffusion of surface-generated •OH radicals toward the lignin anions becomes slower than the direct charge transfer process. This limitation may contribute to the longer degradation times observed. On the other hand, at pH values ≤ 9, lignin solubility decreased and at pH values > 10 lignin solubility was complete. Inwood et al. (2018) showed that the solubility of lignin increases exponentially with pH, with the most effective dissolution occurring at higher pH levels [85]. The ionization of phenolic groups within lignin is a key determinant of its solubility. The apparent pKa values for these groups can vary, but they generally indicate that higher pH levels favor the ionization process, which enhances solubility. The pKa for carboxylic groups has been reported around 5.5, indicating that these groups become increasingly ionized and soluble as pH rises [86].

As a general trend, catalytic activity is greater on soluble substrates than on insoluble substrates. When lignin solubility decreases, it tends to agglomerate, which hinders its interaction with reactive oxygen species. Figure S2A–D illustrates the appearance of the catalyst recovered by centrifugation after the photocatalytic process. The brown coloration of the samples at a pH ≤ 9 suggests the presence of lignin; this generated a decrease in the absorption band of lignin at 290 nm. Therefore, lignin degradation does not take place within the pH range of 5–9. It is important to highlight that black liquor, which is generated during the Kraft pulping process, typically has a high pH, ranging from 12.4 to 12.8 [87]. This alkaline nature of black liquor is significant because it aligns well with the pH requirements for the lignin photodegradation process using ZnO-B_600. Since this pH range does not present a disadvantage, it makes the process highly feasible for industrial applications, where such conditions can be easily maintained. The compatibility between the pH of black liquor and the photodegradation process further underscores

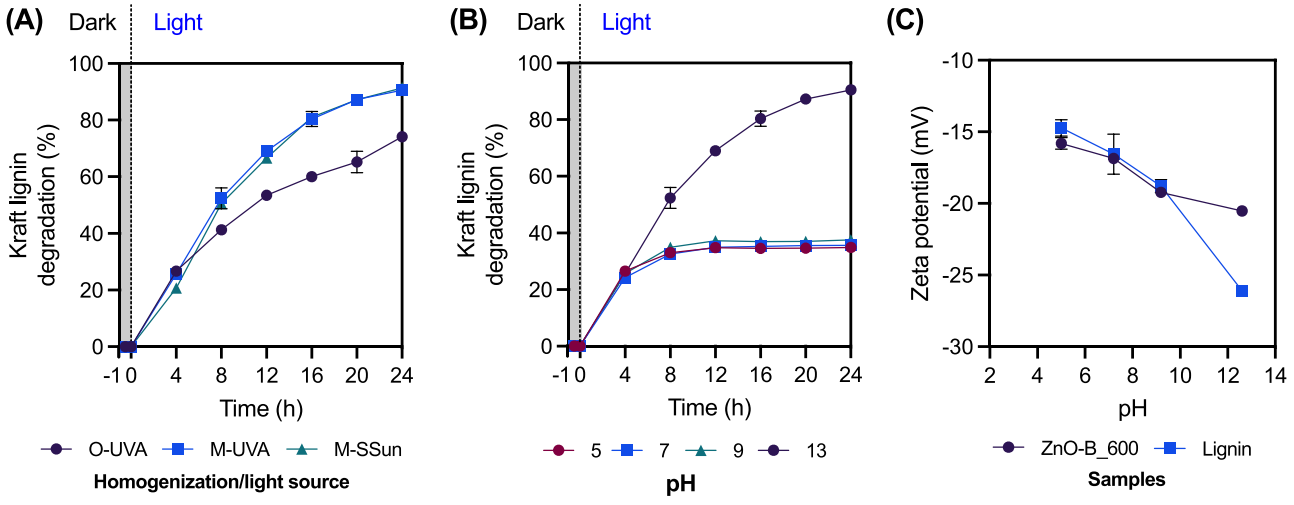

Fig. 7. (A) Photocatalytic degradation (%) of Kraft lignin solution (0.1 g/L) catalyzed by ZnO–B_600 (1 g/L) under different reaction conditions (orbital shaking (O); magnetic stirring (M); UVA radiation (UVA) and simulated sunlight (SSun)) at different time intervals. (B) Influence of pH value on photocatalytic degradation (%) of Kraft lignin using ZnO–B_600. (C) Zeta potential measurement at different pH of ZnO–B_600 and Kraft lignin.

the potential for integrating this technology into existing industrial practices.

3.2.4. Kinetics study of the photocatalytic degradation of lignin

Lignin contains UV–UV-absorbing groups such as phenolic, carbonyl, and other chromophores. The UV absorbance of lignin in the presence of ZnO–B_600 was measured between 200 and 500 nm during 24 h (Fig. 8A). The results exhibit a band absorption of approximately 290 nm, assigned to the non–conjugated phenolic hydroxyl groups present in lignin. As time progresses, the intensity of this absorption band gradually diminishes. The degradation process was also confirmed by observing a change in the color of the Kraft lignin dissolution. Initially, the solution color was dark yellow, which changed to colorless after 24 h of photodegradation.

Fig. 8B illustrates the linear correlation between ln(Ct/C0) and irradiation time for ZnO–B_600, chemically synthesized ZnO, and commercial ZnO. The linear regression analysis confirms that the photocatalytic reactions follow pseudo-first-order kinetics. Among the tested catalysts, ZnO–B_600 displayed the highest rate constant of 0.102 h^{-1}, corresponding to a half-life ($t_{1/2}$) of 6.77 h. In comparison, the rate constant for commercial ZnO (ZnO–C) was 0.069 h^{-1}, while that for chemically synthesized ZnO (ZnO–Ch) was the lowest at 0.012 h^{-1}. These values are lower compared to those reported in the literature. However, the data obtained in this study on ZnO–NPs prepared by a green method are challenging to compare with existing research due to significant differences in factors such as physicochemical properties of ZnO, light source, oxidizing agent, pH medium, lignin source, etc. (Table 3).

3.2.5. Mechanism of lignin photocatalytic degradation

Theoretically, the photocatalytic reaction begins when a semiconductor (in contact with water) is irradiated by light with energy equal to or higher than its band–gap energy, which leads to the promotion of electrons ($e-$) from the valence band (VB) to the conduction band (CB), creating electron/hole pairs ($e-/h+$) [91]. These charge carriers can recombine and be reemitted in the form of light or heat, or they may migrate to the catalyst surface to induce chemical reactions with adsorbed species or near–surface molecules. The photogenerated VB holes can oxidize organic species directly or produce •OH from water molecules adsorbed (donor) on the catalyst surface. Simultaneously, photogenerated CB electrons can be transferred to electron acceptor species, such as molecular oxygen (O_2), to generate superoxide radicals ($\bullet O_2^-$) [91,92]. In the context of lignin depolymerization, these reactive species (•OH and $\bullet O_2^-$) play a critical role in breaking the complex aromatic and aliphatic bonds of lignin molecules. The hydroxyl radicals, in particular, are highly effective at attacking the C–C and C–O bonds within lignin, initiating oxidative cleavage of its macromolecular structure [93]. This process leads to the formation of low-molecular-weight intermediates, such as phenolic monomers or dimers, aldehydes, and organic acids, which are characteristic products of lignin degradation [94]. In the ZnO–mediated photocatalytic system, •OH is the predominately active substance for the oxidation of organic compounds [21,24,95]. According to the literature, •OH produced by photocatalysts can be divided into two types: surface adsorbed •OH (•OHa) and free •OH (•OHf) [96]. Therefore, photocatalysts can not only degrade surface-adsorbed substances but also migrate outwards and react with substances not adsorbed on the surface of catalyst particles [97,98]. In this study, 2–DR was utilized as a reference organic compound to confirm the in-situ generation of hydroxyl radicals by ZnO–B_600 during the photodegradation of lignin (Fig. 8C). The data obtained indicated that •OH radicals were indeed generated from the ZnO–NPs.

Their concentration increased and remained constant throughout the reaction, suggesting a balance between radical consumption and production. This equilibrium likely facilitates continuous oxidative cleavage of lignin, supporting its progressive depolymerization into smaller, more manageable fragments. Additionally, the synergistic effects of superoxide radicals (•O2−) and photogenerated holes ($h+$) further contribute to the oxidative breakdown of lignin's recalcitrant structure, enhancing the overall efficiency of the photodegradation process.

3.2.6. Stability of photocatalysts

The photocatalytic stability of ZnO–NPs poses a limitation for its long–term practical application. In this sense, the stability and reusability of the ZnO–B_600 were evaluated after five consecutive cycles in the photodegradation of lignin. As shown in Fig. 9A and B, the degradation efficacy and rate constants of ZnO exhibit a slight decline (<2%) with an increasing number of cycles, up to five cycles. This reduction is likely attributed to the loss of photocatalyst material during the washing and centrifugation processes. However, these results indicate that ZnO-B_600 is highly stable, retaining its photocatalytic activity over five consecutive cycles. Mushtag et al. (2021) observed similar results, reporting a 4–6% loss of their nanocatalyst (ZnO—Co/N—CNT) after each cycle of use in the depolymerization of Kraft lignin. They also noted a gradual decline in catalytic efficiency with repeated use [99]. Similarly, Zhang et al. (2024) found that using ultra-small ZnO nanoparticles for sodium lignosulfonate depolymerization led to a decrease in the depolymerization rate, dropping to 80% after three cycles and 60% after five cycles [100]. In contrast, our ZnO nanoparticles demonstrated superior stability, with only a 2% reduction in degradation efficiency after five cycles. This minimal loss in performance aligns with findings from other studies, which report that ZnO nanoparticles are highly resistant to corrosion even after multiple cycles of photocatalysis. This resistance likely explains the sustained depolymerization efficiency observed in our tests [101–103].

3.2.6. Identification of the lignin depolymerization products

The lignin photodegradation products generated in the presence of

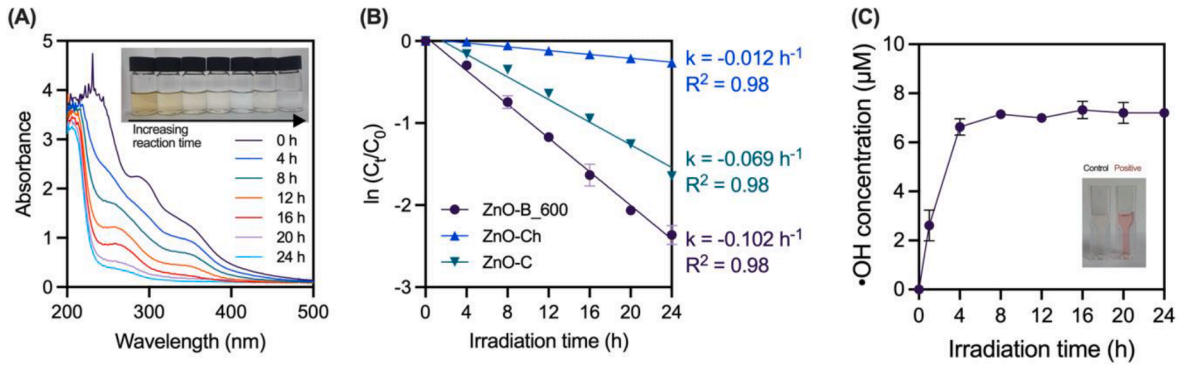

Fig. 8. (A) Change in UV–vis spectra and coloration of Kraft lignin solution (0.1 g/L) during photodegradation using ZnO–B_600. (B) Comparison of reaction kinetics between ZnO-B_600, ZnO—Ch and ZnO—C. (C) Monitoring of •OH concentration during the photodegradation of lignin using ZnO–B_600.

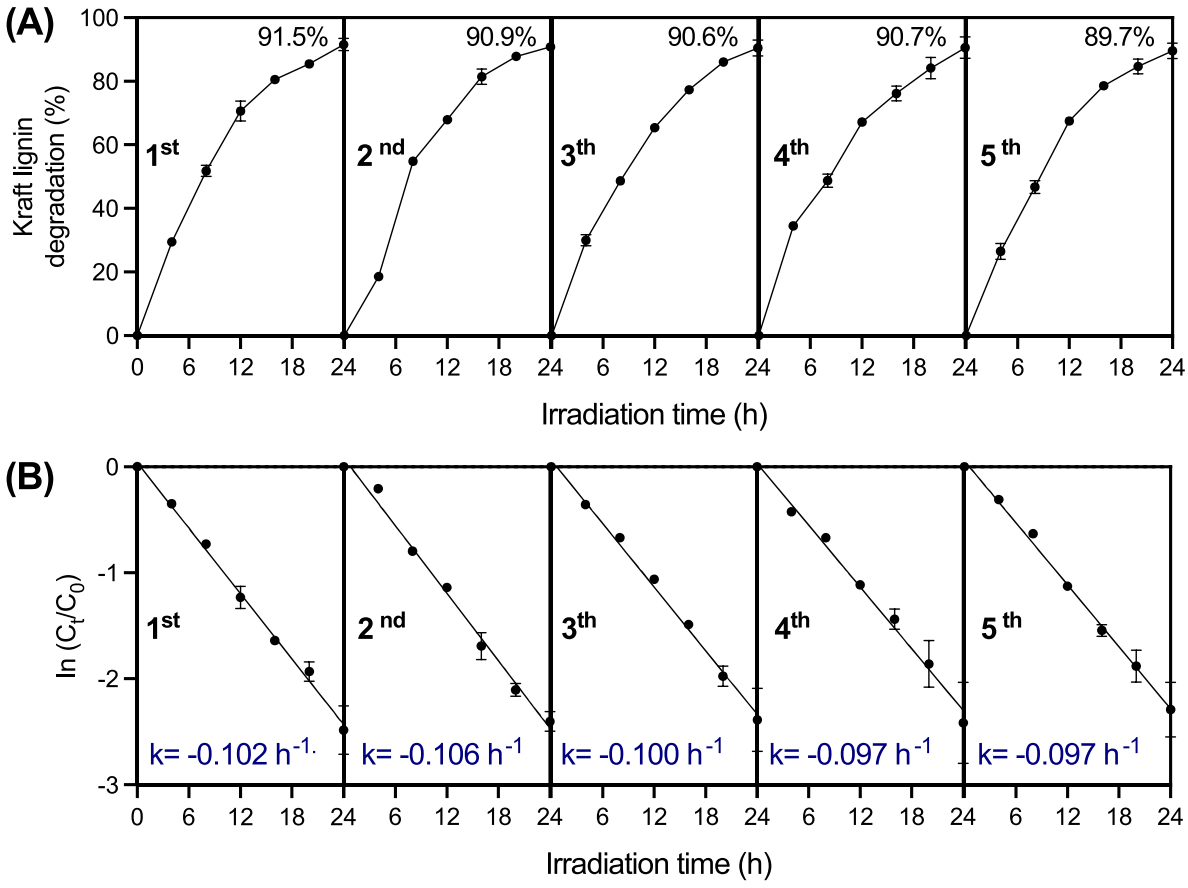

Fig. 9. (A) Degradation of Kraft lignin and (B) reaction kinetics over five consecutive cycles catalyzed by ZnO–B_600.

ZnO–B_600, identified through GC–MS analysis at various reaction times (4, 8, 12, 16, 20, and 24 h), exhibit a clear time-dependent variation. This observation highlights the potential to optimize reaction times to selectively obtain specific target products based on desired outcomes. During the depolymerization of Kraft lignin, both aliphatic and aromatic products are observed. The process, as illustrated in Fig. 10, follows

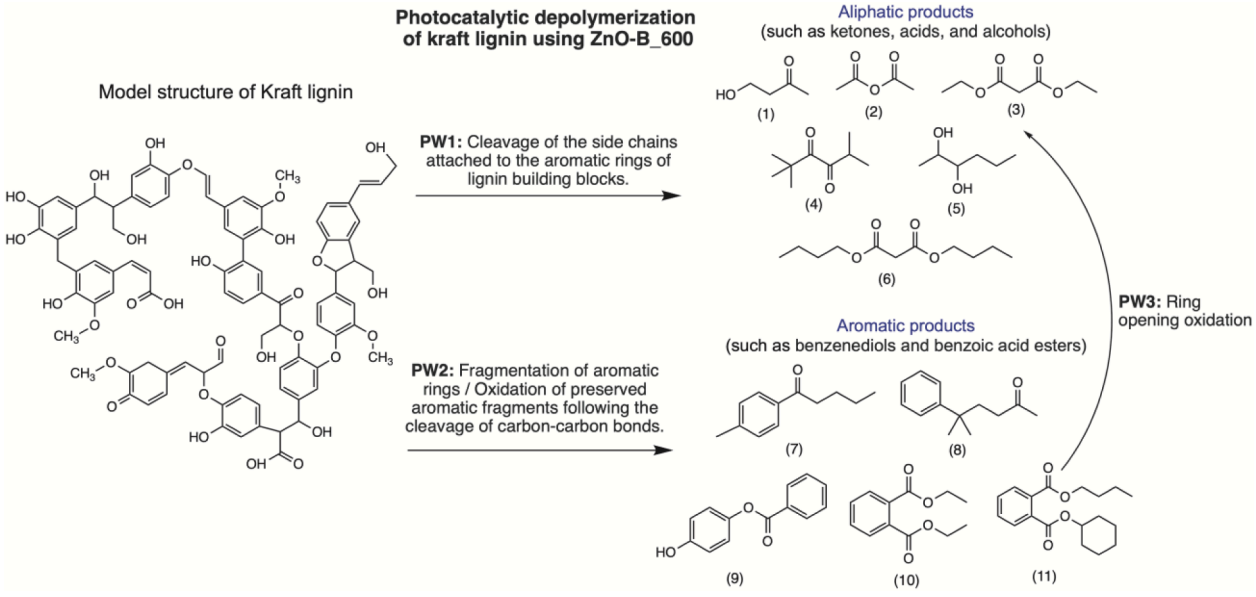

Fig. 10. General pathways proposed for Kraft lignin depolymerization by photocatalytic reactions using ZnO-B_600. Some identified products include: (1) 4-Hydroxybutan-2-one; (2) Acetic anhydride; (3) Diethyl propanedioate; (4) 2,2,5-Trimethylhexane-3,4-dione; (5) 2,3-Hexanediol; (6) Dibutyl propanedioate; (7) 1-(4-Methylphenyl)pentan-1-one; (8) 5-Methyl-5-phenylhexan-2-one; (9) Benzoate of 1,3-benzenediol; (10) Diethyl benzene-1,2-dicarboxylate; (11) Butyl cyclohexyl benzene-1,2-dicarboxylate.

three general pathways. Aliphatic products can be generated through two mechanisms: the cleavage of side chains attached to the aromatic rings of lignin units (PW1) and the oxidative ring opening (PW3). The PW1 pathway involves the breakdown of non-aromatic regions in lignin, resulting in the formation of ketones, acids, and alcohols. In contrast, the PW3 pathway entails the oxidative cleavage of aromatic rings, leading to the production of smaller aliphatic compounds such as diols and carboxylic acids. This mechanism reflects a more advanced stage of lignin oxidation, where the aromatic core is disrupted through oxidative processes, facilitating the release of aliphatic intermediates. On the other hand, aromatic products are formed through the PW2 pathway, which occurs via two mechanisms: fragmentation of the aromatic rings within the lignin structure or oxidation of preserved aromatic fragments following the cleavage of carbon-carbon bonds. The results summarized in Table 4 present the main degradation products obtained at different reaction times during the depolymerization of lignin with ZnO–B_600. The identified signals are primarily associated with ketones, diols, and dicarboxylic acids. At the 4-hour mark, the most abundant product detected was 2,3–hexanediol, indicating the initial cleavage of lignin side chains and the predominance of aliphatic compounds. After 8 h, the signal for 1,2–benzenedicarboxylic acid diethyl ester became significant, suggesting a transition towards aromatic products. At 12 and 16 h, compounds such as phthalic acid cyclobutyl isobutyl ester were observed, reflecting further oxidation and fragmentation of aromatic structures. By 20 h, the presence of 2–(1–oxopropyl)–benzoic acid and 4–hydroxy–2–butanone indicated advanced stages of oxidation and ring-opening processes. The shift in product distribution over time highlights the sequential nature of lignin depolymerization. Initially, the cleavage of side chains leads to the formation of aliphatic products, while prolonged reaction times (>8 h) favor the oxidation and fragmentation of aromatic rings, yielding aromatic derivatives.

From a Kraft lignin valorization perspective, it is important to note that all detected depolymerization products, as shown in Table 4, are high-value chemicals with applications in the production of plastics, insecticides, cosmetics, and pharmaceuticals [104–106]. This finding emphasizes the potential of the photocatalytic process to generate valuable compounds from the depolymerization of Kraft lignin for diverse industrial applications.

4. Conclusion

ZnO–NP catalysts were successfully synthesized using *A. chilensis* plant extract and subjected to different calcination temperatures. Among the prepared catalysts, ZnO–B_600 exhibited the highest lignin degradation efficiency, achieving 91% after 24 h of photocatalytic treatment. The photocatalytic activity of ZnO–B_600 was significantly influenced by chemical parameters—such as the pH of the reaction medium and the synthesis method of ZnO–NPs—as well as physical parameters, including the type of radiation and stirring applied during the process. The lignin degradation resulted in the formation of various high-value products, whose composition changed over time. This suggests the potential to develop strategies for optimizing reaction times to selectively obtain specific products of interest. These findings highlight the potential of photocatalytic technologies as a promising and practical approach for sustainable Kraft pulping waste management and the production of value-added chemicals for industries such as chemicals, pharmaceuticals, and cosmetics. Future research should focus on scaling up the process for industrial applications, optimizing photocatalytic systems to enhance efficiency and product selectivity on a larger scale, and evaluating simpler lignin models to advance a better understanding of the specific reactions catalyzed by ZnO–B_600.

CRediT authorship contribution statement

Joelis Vera: Writing – review & editing, Writing – original draft, Visualization, Validation, Software, Methodology, Investigation, Formal analysis, Conceptualization. **Wence Herrera:** Writing – review & editing, Methodology, Investigation, Formal analysis, Conceptualization. **Edward Hermosilla:** Writing – review & editing, Supervision, Resources, Methodology, Investigation, Conceptualization. **Heidi Schalchli:** Writing – review & editing, Methodology, Investigation. **Ramiro Díaz:** Writing – review & editing, Methodology, Investigation, Funding acquisition, Formal analysis, Data curation. **Paola Fincheira:** Writing – review & editing, Visualization, Validation, Investigation. **Amedea B.**

Table 4
Products detected during the photocatalytic lignin degradation using ZnO–B_600 at different reaction time intervals.

No.	Name	Time (h)						Retention Time (min)	RI*	RI**	Relative area (%)	Function
		4	8	12	16	20	24					
1	2–Butanone, 4–hydroxy						•	3.03	745	798	68.8	Preparation of species with pharmaceutical activity
2	Acetic anhydride	•	•	•		•		3.51	770	722	0.4 – 1.3	Manufacturing of plastic, pharmaceuticals, perfumes and dyes
3	Oxalic acid, ethyl propyl ester		•			•		8.93	1063	1052	0.3 – 1.3	Synthetic intermediates used in the pharmaceutical industry
4	3,4–Hexanedione, 2,2,5–trimethyl					•		9.54	1098	1039	1.3 – 16.5	—
5	1–Pentanone, 1–(4–methyl phenyl)			•		•		9.96	1124	1440	1.5 – 6.7	Flavor enhancer and aroma ingredient used in the food industry
6	RS–2,3–hexanediol	•	•		•	•	•	10.15	1136	942	0.5 – 9.0	Plasticizers in the plastic and resin industry
7	2–Hexanone, 5–methyl–5–phenyl					•		10.49	1158	1442	2.5	Manufacturing of biocide fragrances, cosmetics, and personal care products
8	Oxalic acid, butyl propyl ester		•	•			•	11.13	1198	1250	2.4 – 20.0	—
9	(SS) – or (RR)–2,3–hexanediol	•	•	•	•		•	12.65	1302	942	0.7 – 11.0	Synthesis of different compounds like plasticizers, humectant and solvents
10	1,3–Benzenediol, monobenzoate		•			•		19.33	1711	1855	2.9 – 3.6	UV inhibitors added mainly to outdoor plastics and color stabilizers in cosmetic compositions
11	1,2–Benzenedicarboxylic acid, diethyl ester		•	•				17.23	1594	1598	56.3 – 77.8	Production of insecticides and cosmetics
12	1,2–Benzenedicarboxylic acid, butyl cyclohexyl ester				•			28.79	2249	2299	20.1	Manufacturing of personal care products, medical and household applications

The identification of compounds was determined by comparison of the retention index (RI) and also from the Mass spectrum (MS) of each component with NIST08 and NIST08s database.
RI* = Retention index relative to *n*–alkanes C7–C30 standard (Supelco 49451–U) in an HP–5MS capillary column.
RI** (RI Teor) = Retention index obtained from database NIST08 and NIST08s.

Seabra: Writing – review & editing, Visualization, Validation, Supervision, Resources, Methodology. **Andrés Quiroz:** Writing – review & editing, Investigation, Formal analysis, Data curation. **Gonzalo Tortella:** Writing – review & editing, Supervision, Methodology, Investigation. **Olga Rubilar:** Writing – review & editing, Writing – original draft, Validation, Supervision, Resources, Methodology, Conceptualization.

Declaration of competing interest

The authors declare the following financial interests/personal relationships which may be considered as potential competing interests:

Olga Rubilar reports financial support was provided by Universidad de La Frontera. Olga Rubilar reports financial support was provided by ANID FONDAP. Edward Hermosilla reports financial support was provided by ANID FONDECYT. Amedea B. Seabra reports financial support was provided by Fundação de amparo à pesquisa do Estado de São Paulo (Fapesp). If there are other authors, they declare that they have no known competing financial interests or personal relationships that could have appeared to influence the work reported in this paper.

Acknowledgments

This research was funded by the following sources: the ANID doctoral scholarship 21211180, ANID/FONDAP 15130015, ANID/FONDAP/1523A0001, Universidad de La Frontera DI23–3002, Universidad de La Frontera PP23–0046, Universidad de La Frontera DI23–10002, ANID FONDECYT Iniciación 11230939, and the Fundação de Amparo à Pesquisa do Estado de São Paulo (FAPESP) under process numbers 2022/00321–0 (ABS) and 2022/13444-3 (da Silva LL) projects.

Supplementary materials

Supplementary material associated with this article can be found, in the online version, at doi:10.1016/j.rineng.2024.103866.

Data availability

Data will be made available on request.

References

[1] F.G. Calvo-Flores, J.A. Dobado, J. Isac-García, F.J. Martín-Martínez, Lignin and Lignans as Renewable Raw Materials: chemistry, Technology and Applications, 2015. https://doi.org/10.1002/9781118682784.

[2] C. Chio, M. Sain, W. Qin, Lignin utilization: a review of lignin depolymerization from various aspects, Renew. Sustain. Energy Rev. 107 (2019) 232–249, https://doi.org/10.1016/J.RSER.2019.03.008.

[3] S. Guadix-Montero, M. Sankar, Review on catalytic cleavage of C–C inter-unit linkages in lignin model compounds: towards lignin depolymerisation, Top. Catal. (2018) 61, https://doi.org/10.1007/s11244-018-0909-2.

[4] ARAUCO, (n.d.). https://arauco.com/mo/wp-content/uploads/sites/25/2017/07/Sustaintability-Report-2009.pdf (accessed December 15, 2024).

[5] CMPC S.A. - Financials - Annual Reports, (n.d.). https://ir.cmpc.com/English/financials/annual-reports/default.aspx (accessed December 15, 2024).

[6] S. Gillet, M. Aguedo, L. Petitjean, A.R.C. Morais, A.M. Da Costa Lopes, R. M. Łukasik, P.T. Anastas, Lignin transformations for high value applications: towards targeted modifications using green chemistry, Green Chem. 19 (2017) 4200–4233, https://doi.org/10.1039/C7GC01479A.

[7] I.C. Belo, R.C.P. Oliveira, M. Mateus, J.C.M. Bordado, P. Pinto, D.M.F. Santos, Development of a black liquor electrolyzer for lignin extraction, ECS Trans. 86 (2018) 3–9, https://doi.org/10.1149/08604.0003ECST/XML.

[8] D.S. Bajwa, G. Pourhashem, A.H. Ullah, S.G. Bajwa, A concise review of current lignin production, applications, products and their environmental impact, Ind. Crops. Prod. 139 (2019) 111526, https://doi.org/10.1016/J.INDCROP.2019.111526.

[9] S. Sharma, A. Sharma, S.I. Mulla, D. Pant, T. Sharma, A. Kumar, Lignin as potent industrial biopolymer: an introduction, (2020) 1–15. https://doi.org/10.1007/978-3-030-40663-9_1.

[10] R. Abejón, H. Pérez-Acebo, L. Clavijo, Alternatives for chemical and biochemical lignin valorization: hot topics from a bibliometric analysis of the research published during the 2000–2016 period, Processes 6 (2018), https://doi.org/10.3390/pr6080098.

[11] E. Liu, M.I.V. Mercado, F. Segato, M.R. Wilkins, A green pathway for lignin valorization: enzymatic lignin depolymerization in biocompatible ionic liquids and deep eutectic solvents, Enzyme Microb. Technol. 174 (2024) 110392, https://doi.org/10.1016/J.ENZMICTEC.2023.110392.

[12] D. Bourbiaux, J. Pu, F. Rataboul, L. Djakovitch, C. Geantet, D. Laurenti, Reductive or oxidative catalytic lignin depolymerization: an overview of recent advances, Catal. Today 373 (2021) 24–37, https://doi.org/10.1016/J.CATTOD.2021.03.027.

[13] L. Cao, I.K.M. Yu, Y. Liu, X. Ruan, D.C.W. Tsang, A.J. Hunt, Y.S. Ok, H. Song, S. Zhang, Lignin valorization for the production of renewable chemicals: state-of-the-art review and future prospects, Bioresour. Technol. 269 (2018) 465–475, https://doi.org/10.1016/J.BIORTECH.2018.08.065.

[14] Y. Cao, S.S. Chen, S. Zhang, Y.S. Ok, B.M. Matsagar, K.C.W. Wu, D.C.W. Tsang, Advances in lignin valorization towards bio-based chemicals and fuels: lignin biorefinery, Bioresour. Technol. 291 (2019) 121878, https://doi.org/10.1016/J.BIORTECH.2019.121878.

[15] H. Wang, M. Tucker, Y. Ji, Recent development in chemical depolymerization of lignin: a review, J. Appl. Chem. 2013 (2013) 838645, https://doi.org/10.1155/2013/838645.

[16] V. Kumar, M.P. Shah, Advanced oxidation processes for complex wastewater treatment, Adv. Oxid. Process. Effluent Treat. Plants (2021) 1–31, https://doi.org/10.1016/B978-0-12-821011-6.00001-3.

[17] R. Dewil, D. Mantzavinos, I. Poulios, M.A. Rodrigo, New perspectives for advanced oxidation processes, J. Environ. Manage 195 (2017) 93–99, https://doi.org/10.1016/J.JENVMAN.2017.04.010.

[18] K. Qi, B. Cheng, J. Yu, W. Ho, Review on the improvement of the photocatalytic and antibacterial activities of ZnO, J. Alloys. Compd. 727 (2017) 792–820, https://doi.org/10.1016/J.JALLCOM.2017.08.142.

[19] M. Martínez-Carmona, Y. Gun'Ko, M. Vallet-Regí, ZnO nanostructures for drug delivery and theranostic applications, Nanomaterials 8 (2018) 268, https://doi.org/10.3390/NANO8040268.

[20] A. Singh, N.B. Singh, S. Afzal, T. Singh, I. Hussain, Zinc oxide nanoparticles: a review of their biological synthesis, antimicrobial activity, uptake, translocation and biotransformation in plants, J. Mater. Sci. 53 (2018) 185–201, https://doi.org/10.1007/S10853-017-1544-1/METRICS.

[21] S.K. Kansal, M. Singh, D. Sud, Studies on TiO2/ZnO photocatalysed degradation of lignin, J. Hazard. Mater. 153 (2008) 412–417, https://doi.org/10.1016/J.JHAZMAT.2007.08.091.

[22] M. Mazarji, M. Alvarado-Morales, P. Tsapekos, G. Nabi-Bidhendi, N. M. Mahmoodi, I. Angelidaki, Graphene based ZnO nanoparticles to depolymerize lignin-rich residues via UV/iodide process, Environ. Int. 125 (2019) 172–183, https://doi.org/10.1016/j.envint.2018.12.062.

[23] J. Xu, M. Li, L. Yang, J. Qiu, Q. Chen, X. Zhang, Y. Feng, J. Yao, Synergy of Ni dopant and oxygen vacancies in ZnO for efficient photocatalytic depolymerization of sodium lignosulfonate, Chem. Eng. J. 394 (2020) 125050, https://doi.org/10.1016/J.CEJ.2020.125050.

[24] S. Lenka, S.K. Badamali, Nanostructured ZnO as an efficient heterogeneous photocatalyst towards degradation of lignin under visible light irradiation, Mol. Catal. 536 (2023) 112918, https://doi.org/10.1016/J.MCAT.2023.112918.

[25] A.P. Reverberi, D.M. D'Addona, A.A.G. Bruzzone, R. Teti, B. Fabiano, Nanotechnology in machining processes: recent advances, Procedia CIRP 79 (2019) 3–8, https://doi.org/10.1016/J.PROCIR.2019.02.002.

[26] A.A. Ramanathan, M.W. Aqra, An Overview of the Green Road to the Synthesis of Nanoparticles, J. Mater. Sci. Res. Rev. 2 (2019) 114–124, https://doi.org/10.9734/JMSRR/2019/V2I137.

[27] S. Lal, P.L. Nayak, Green synthesis of gold nanoparticles using various extract of plants and spices, Int. J. Sc. Innov. Discov. 2 (2012).

[28] M. Ovais, A.T. Khalil, N.U. Islam, I. Ahmad, M. Ayaz, M. Saravanan, Z. K. Shinwari, S. Mukherjee, Role of plant phytochemicals and microbial enzymes in biosynthesis of metallic nanoparticles, Appl. Microbiol. Biotechnol. 102 (2018) 6799–6814, https://doi.org/10.1007/S00253-018-9146-7.

[29] T. Liang, W. Yue, Q. Li, Comparison of the phenolic content and antioxidant activities of Apocynum venetum L. (Luo-Bu-Ma) and two of its alternative species, Int. J. Mol. Sci. 11 (2010) 4452–4464, https://doi.org/10.3390/IJMS11114452.

[30] K. Shivaji, E.S. Monica, A. Devadoss, D.D. Kirubakaran, C.R. Dhas, S.M. Jain, S. Pitchaimuthu, Synthesizing green photocatalyst using plant leaf extract for water pollutant treatment, (2020) 25–46. https://doi.org/10.1007/978-3-030-15608-4_2.

[31] D. Sharma, S. Kanchi, K. Bisetty, Biogenic synthesis of nanoparticles: a review, Arab. J. Chem. 12 (2019) 3576–3600, https://doi.org/10.1016/J.ARABJC.2015.11.002.

[32] S. Zinatloo-Ajabshir, M. Ahmadi-Zeidabadi, M. Amiri, F. Sharifianjazi, Innovative sono-synthesis of cerium dioxide nanomaterials using mentha extract with efficient activity for cancer therapy application, Results. Eng. 23 (2024) 102720, https://doi.org/10.1016/J.RINENG.2024.102720.

[33] S. Zinatloo-Ajabshir, M.S. Morassaei, M. Salavati-Niasari, Eco-friendly synthesis of Nd2Sn2O7–based nanostructure materials using grape juice as green fuel as photocatalyst for the degradation of erythrosine, Compos. B Eng. 167 (2019) 643–653, https://doi.org/10.1016/J.COMPOSITESB.2019.03.045.

[34] M. Ovais, A.T. Khalil, M. Ayaz, I. Ahmad, S.K. Nethi, S. Mukherjee, Biosynthesis of metal nanoparticles via microbial enzymes: a mechanistic approach, Int. J. Mol. Sci. 19 (2018) 4100, https://doi.org/10.3390/IJMS19124100.

[35] J. Singh, T. Dutta, K.H. Kim, M. Rawat, P. Samddar, P. Kumar, 'Green' synthesis of metals and their oxide nanoparticles: applications for environmental remediation, J. Nanobiotechnol. 16 (2018) 1–24, https://doi.org/10.1186/S12951-018-0408-4.

[36] S. Zeghoud, H. Hemmami, B. Ben Seghir, I. Ben Amor, I. Kouadri, A. Rebiai, M. Messaoudi, S. Ahmed, P. Pohl, J. Simal-Gandara, A review on biogenic green synthesis of ZnO nanoparticles by plant biomass and their applications, Mater. Today Commun. 33 (2022) 104747, https://doi.org/10.1016/J.MTCOMM.2022.104747.
[37] S.A. Akintelu, A.S. Folorunso, A review on green synthesis of zinc oxide nanoparticles using plant extracts and its biomedical applications, Bionanoscience 10 (2020) 848–863, https://doi.org/10.1007/S12668-020-00774-6/METRICS.
[38] S. Ahmed, Annu, S.A. Chaudhry, S. Ikram, A review on biogenic synthesis of ZnO nanoparticles using plant extracts and microbes: a prospect towards green chemistry, J. Photochem. Photobiol. B 166 (2017) 272–284, https://doi.org/10.1016/J.JPHOTOBIOL.2016.12.011.
[39] G.E. Zúñiga, A. Tapia, A. Arenas, R.A. Contreras, G. Zúñiga-Libano, Phytochemistry and biological properties of Aristotelia chilensis a Chilean blackberry: a review, Phytochem. Rev. 16 (2017) 1081–1094, https://doi.org/10.1007/S11101-017-9533-1/FIGURES/10.
[40] J. Vera, W. Herrera, E. Hermosilla, M. Díaz, J. Parada, A.B. Seabra, G. Tortella, H. Pesenti, G. Ciudad, O. Rubilar, Antioxidant activity as an indicator of the efficiency of plant extract-mediated synthesis of zinc oxide nanoparticles, Antioxidants 12 (2023), https://doi.org/10.3390/antiox12040784.
[41] J. Vera, W. Herrera, E. Hermosilla, M. Díaz, J. Parada, A.B. Seabra, G. Tortella, H. Pesenti, G. Ciudad, O. Rubilar, Antioxidant activity as an indicator of the efficiency of plant extract-mediated synthesis of zinc oxide nanoparticles, Antioxidants 12 (2023) 784, https://doi.org/10.3390/ANTIOX12040784.
[42] K.A. Crisóstomo-Ayala, A.B. Sabater-Jara, C.P. Manriquez, F. Ferreres, Á. Gil-Izquierdo, M.Á. Pedreño, M.H. de la Torre, M. Sanchez-Olate, D.G.R. Leal, Comparative study of metabolomic profile and antioxidant content of adult and in vitro leaves of aristotelia Chilensis, Plants 11 (2022) 37, https://doi.org/10.3390/PLANTS11010037/S1.
[43] J.L. Vidal, L.M. Avello, C.C. Loyola, P.J. Campos, M.P. Aqueveque, R.S. Dungan, L.M. Galotto, M.A. Guarda, Microencapsulation of maqui (Aristotelia chilensis Molina Stuntz) leaf extracts to preserve and control antioxidant properties, Chil. J. Agric. Res. 73 (2013) 17–23, https://doi.org/10.4067/S0718-58392013000100003.
[44] N. Sedefoglu, Green synthesis of ZnO nanoparticles by Myrtus communis plant extract with investigation of effect of precursor, calcination temperature and study of photocatalytic performance, Ceram. Int. 50 (2024), https://doi.org/10.1016/j.ceramint.2024.01.387.
[45] A. Rasool, S. Kiran, T. Gulzar, S. Abrar, A. Ghaffar, M. Shahid, S. Nosheen, S. Naz, Biogenic synthesis and characterization of ZnO nanoparticles for degradation of synthetic dyes: a sustainable environmental cleaner approach, J. Clean. Prod. 398 (2023) 136616, https://doi.org/10.1016/J.JCLEPRO.2023.136616.
[46] K. Singh, Nancy, J. Singh, G. Singh, Efficient photocatalytic degradation of industrial dye using biogenic ZnO NPs, Mater. Today Proc. 68 (2022) 760–765, https://doi.org/10.1016/J.MATPR.2022.06.138.
[47] V. Koutu, L. Shastri, M.M. Malik, Effect of NaOH concentration on optical properties of zinc oxide nanoparticles, Mater. Sci.- Poland 34 (2016) 819–827, https://doi.org/10.1515/MSP-2016-0119.
[48] N. Srisasiwimon, S. Chuangchote, N. Laosiripojana, T. Sagawa, TiO2/Lignin-Based carbon composited photocatalysts for enhanced photocatalytic conversion of lignin to high value chemicals, ACS Sustain. Chem. Eng. 6 (2018) 13968–13976, https://doi.org/10.1021/ACSSUSCHEMENG.8B02353/ASSET/IMAGES/MEDIUM/SC-2018-023532_0010.GIF.
[49] H. Li, Z. Lei, C. Liu, Z. Zhang, B. Lu, Photocatalytic degradation of lignin on synthesized Ag–AgCl/ZnO nanorods under solar light and preliminary trials for methane fermentation, Bioresour. Technol. 175 (2015) 494–501, https://doi.org/10.1016/J.BIORTECH.2014.10.143.
[50] J. Kou, C. Lu, J. Wang, Y. Chen, Z. Xu, R.S. Varma, Selectivity enhancement in heterogeneous photocatalytic transformations, Chem. Rev. 117 (2017) 1445–1514, https://doi.org/10.1021/acs.chemrev.6b00396.
[51] M.C. Krueger, U. Hofmann, M. Moeder, D. Schlosser, Potential of wood-rotting fungi to attack polystyrene sulfonate and its depolymerisation by Gloeophyllum trabeum via hydroquinone-driven Fenton chemistry, PLoS One 10 (2015) e0131773, https://doi.org/10.1371/JOURNAL.PONE.0131773.
[52] Y. Yang, S. Ghatge, Y. Ko, Y. Yoon, J.H. Ahn, J.J. Kim, H.G. Hur, Non-specific degradation of chloroacetanilide herbicides by glucose oxidase supported Bio-Fenton reaction, Chemosphere 292 (2022) 133417, https://doi.org/10.1016/J.CHEMOSPHERE.2021.133417.
[53] E. Marco-Urrea, E. Aranda, G. Caminal, F. Guillén, Induction of hydroxyl radical production in Trametes versicolor to degrade recalcitrant chlorinated hydrocarbons, Bioresour. Technol. 100 (2009) 5757–5762, https://doi.org/10.1016/J.BIORTECH.2009.06.078.
[54] S. Karthikeyan, G. Sekaran, In situ generation of a hydroxyl radical by nanoporous activated carbon derived from rice husk for environmental applications: kinetic and thermodynamic constants, Phys. Chem. Chem. Phys. 16 (2014) 3924–3933, https://doi.org/10.1039/C3CP54185A.
[55] M. Rana, G. Taki, M.N. Islam, A. Agarwal, Y.T. Jo, J.H. Park, Effects of temperature and salt catalysts on depolymerization of kraft lignin to aromatic phenolic compounds, Energy Fuels 33 (2019) 6390–6404, https://doi.org/10.1021/ACS.ENERGYFUELS.9B00808/ASSET/IMAGES/MEDIUM/EF-2019-00808K_0008.GIF.
[56] J. Fernández-Rodríguez, X. Erdocia, C. Sánchez, M. González Alriols, J. Labidi, Lignin depolymerization for phenolic monomers production by sustainable processes, J. Energy Chem. 26 (2017) 622–631, https://doi.org/10.1016/J.JECHEM.2017.02.007.
[57] R.P. Adams, Identification of Essential Oil Components by Gas Chromatography/Mass Spectrometry, 4th ed., Allured, Carol Stream, IL, 2007.
[58] V.I. Babushok, P.J. Linstrom, I.G. Zenkevich, Retention indices for frequently reported compounds of plant essential oils, J. Phys. Chem. Ref. Data 40 (2011) 043101, https://doi.org/10.1063/1.3653552.
[59] Pherobase, Kovats Retention Index, (2024). https://www.pherobase.com/database/kovats/kovats-detail-4-pentenylbutyrate.php.
[60] A. Jayachandran, A. T.R, A.S. Nair, Green synthesis and characterization of zinc oxide nanoparticles using Cayratia pedata leaf extract, Biochem. Biophys. Rep. 26 (2021) 100995, https://doi.org/10.1016/J.BBREP.2021.100995.
[61] R. Sharma, R. Garg, A. Kumari, A review on biogenic synthesis, applications and toxicity aspects of zinc oxide nanoparticles, EXCLI J. 19 (2020) 1325, https://doi.org/10.17179/EXCLI2020-2842.
[62] T. Tatarchuk, A. Peter, B. Al-Najar, J. Vijaya, M. Bououdina, Photocatalysis: activity of Nanomaterials, Nanotechnol. Environ. Sci. 1–2 (2018) 209–292, https://doi.org/10.1002/9783527808854.CH8.
[63] P. Peerakiatkhajohn, T. Butburee, J.H. Sul, S. Thaweesak, J.H. Yun, Efficient and rapid photocatalytic degradation of methyl orange dye using Al/ZnO nanoparticles, Nanomaterials 11 (2021) 1059, https://doi.org/10.3390/NANO11041059.
[64] A. Umar, R. Kumar, G. Kumar, H. Algarni, S.H. Kim, Effect of annealing temperature on the properties and photocatalytic efficiencies of ZnO nanoparticles, J. Alloys. Compd. 648 (2015) 46–52, https://doi.org/10.1016/J.JALLCOM.2015.04.236.
[65] D. Tromans, J.A. Meech, Enhanced dissolution of minerals: stored energy, amorphism and mechanical activation, Miner. Eng. 14 (2001) 1359–1377, https://doi.org/10.1016/S0892-6875(01)00151-0.
[66] A. Khorsand Zak, W.H. Abd. Majid, M.E. Abrishami, R. Yousefi, X-ray analysis of ZnO nanoparticles by Williamson–Hall and size–strain plot methods, Solid State Sci. 13 (2011) 251–256, https://doi.org/10.1016/J.SOLIDSTATESCIENCES.2010.11.024.
[67] M. Naeem, S. Qaseem, I.H. Gul, A. Maqsood, Study of active surface defects in Ti doped ZnO nanoparticles, J. Appl. Phys. 107 (2010), https://doi.org/10.1063/1.3432571/146346.
[68] I.S. Okeke, K.K. Agwu, A.A. Ubachukwu, I.G. Madiba, M. Maaza, G.M. Whyte, F. I. Ezema, Impact of particle size and surface defects on antibacterial and photocatalytic activities of undoped and Mg-doped ZnO nanoparticles, biosynthesized using one-step simple process, Vacuum 187 (2021) 110110, https://doi.org/10.1016/J.VACUUM.2021.110110.
[69] L.H. Hashim, A. Halilu, Y.B. Umar, M.R. Bin Johan, M.K. Aroua, P. Koley, S. K. Bhargava, Role of lattice strain in bifunctional catalysts for tandem furfural hydrogenation–esterification, Catal. Sci. Technol. 13 (2023) 774–787, https://doi.org/10.1039/D2CY01929A.
[70] M.A. Vergés, A. Mifsud, C.J. Serna, Formation of rod-like zinc oxide microcrystals in homogeneous solutions, J. Chem. Soc. Faraday Trans. 86 (1990) 959–963, https://doi.org/10.1039/FT9908600959.
[71] K. Raja, P.S. Ramesh, D. Geetha, Synthesis, structural and optical properties of ZnO and Ni-doped ZnO hexagonal nanorods by Co-precipitation method, Spectrochim. Acta A Mol. Biomol. Spectrosc. 120 (2014) 19–24, https://doi.org/10.1016/J.SAA.2013.09.103.
[72] H. Ahmad, K. Venugopal, K. Rajagopal, S. De Britto, B. Nandini, H. G. Pushpalatha, N. Konappa, A.C. Udayashankar, N. Geetha, S. Jogaiah, Green synthesis and characterization of zinc oxide nanoparticles using eucalyptus globules and their fungicidal ability against pathogenic fungi of apple orchards, Biomolecules 10 (2020) 425, https://doi.org/10.3390/BIOM10030425.
[73] E.F. El-Belely, M.M.S. Farag, H.A. Said, A.S. Amin, E. Azab, A.A. Gobouri, A. Fouda, Green synthesis of zinc oxide nanoparticles (ZnO-NPs) using Arthrospira platensis (Class: Cyanophyceae) and evaluation of their biomedical activities, Nanomaterials 11 (2021) 95, https://doi.org/10.3390/NANO11010095.
[74] T.U. Doan Thi, T.T. Nguyen, Y.D. Thi, K.H. Ta Thi, B.T. Phan, K.N. Pham, Green synthesis of ZnO nanoparticles using orange fruit peel extract for antibacterial activities, RSC Adv. 10 (2020) 23899–23907, https://doi.org/10.1039/D0RA04926C.
[75] A. Hawe, W.L. Hulse, W. Jiskoot, R.T. Forbes, Taylor dispersion analysis compared to dynamic light scattering for the size analysis of therapeutic peptides and proteins and their aggregates, Pharm. Res. 28 (2011) 2302–2310, https://doi.org/10.1007/S11095-011-0460-3/TABLES/2.
[76] H. Yin, V.A. Coleman, P.S. Casey, B. Angel, H.J. Catchpoole, L. Waddington, M. J. McCall, A comparative study of the physical and chemical properties of nano-sized ZnO particles from multiple batches of three commercial products, J. Nanopart. Res. 17 (2015) 1–19, https://doi.org/10.1007/S11051-014-2851-Y/FIGURES/5.
[77] M. Danaei, M. Dehghankhold, S. Ataei, F. Hasanzadeh Davarani, R. Javanmard, A. Dokhani, S. Khorasani, M.R. Mozafari, Impact of particle size and polydispersity index on the clinical applications of lipidic nanocarrier systems, Pharmaceutics 10 (2018) 57, https://doi.org/10.3390/PHARMACEUTICS10020057.
[78] K.G. Kornev, Y. Gu, P. Aprelev, A. Tokarev, Magnetic rotational spectroscopy for probing rheology of nanoliter droplets and thin films, magnetic characterization techniques for nanomaterials (2017) 51–83. https://doi.org/10.1007/978-3-662-52780-1_2.
[79] J. Iqbal, B.A. Abbasi, T. Yaseen, S.A. Zahra, A. Shahbaz, S.A. Shah, S. Uddin, X. Ma, B. Raouf, S. Kanwal, W. Amin, T. Mahmood, H.A. El-Serehy, P. Ahmad, Green synthesis of zinc oxide nanoparticles using Elaeagnus angustifolia L. leaf

extracts and their multiple in vitro biological applications, Sci. Rep. 11 (2021) 1–13, https://doi.org/10.1038/s41598-021-99839-z.
[80] E. Joseph, G. Singhvi, Multifunctional nanocrystals for cancer therapy: a potential nanocarrier, Nanomater. Drug Deliv. Ther. (2019) 91–116, https://doi.org/10.1016/B978-0-12-816505-8.00007-2.
[81] S.S. Mkhize, O.J. Pooe, S. Khoza, I.N. Mongalo, R. Khan, M.B.C. Simelane, Characterization and biological evaluation of zinc oxide nanoparticles synthesized from Pleurotus ostreatus Mushroom, Appl. Sci. 12 (2022) 8563, https://doi.org/10.3390/APP12178563.
[82] R. Marsalek, Particle size and zeta potential of ZnO, APCBEE Procedia 9 (2014) 13–17, https://doi.org/10.1016/J.APCBEE.2014.01.003.
[83] A.H. Zyoud, A. Zubi, S.H. Zyoud, M.H. Hilal, S. Zyoud, N. Qamhieh, A. R. Hajamohideen, H.S. Hilal, Kaolin-supported ZnO nanoparticle catalysts in self-sensitized tetracycline photodegradation: zero-point charge and pH effects, Appl. Clay. Sci. 182 (2019), https://doi.org/10.1016/j.clay.2019.105294.
[84] H. Wang, C. Xie, W. Zhang, S. Cai, Z. Yang, Y. Gui, Comparison of dye degradation efficiency using ZnO powders with various size scales, J. Hazard. Mater. 141 (2007), https://doi.org/10.1016/j.jhazmat.2006.07.021.
[85] J.P.W. Inwood, L. Pakzad, P. Fatehi, Production of sulfur containing kraft lignin products, Bioresources 13 (2018), https://doi.org/10.15376/biores.13.1.53-70.
[86] T. Sewring, J. Durruty, L. Schneider, H. Schneider, T. Mattsson, H. Theliander, Acid precipitation of kraft lignin from aqueous solutions: the influence of pH, temperature, and Xylan, J. Wood Chem. Technol. 39 (2019), https://doi.org/10.1080/02773813.2018.1488870.
[87] N.A. Sadiku, A.F. Yusuph, N.A. Sadiku, A.F. Yusuph, Characterisation of lignins isolated from Bamboo organosolv and kraft black liquor, Maderas, Ciencia y Tecnología 25 (2023) 15–16, https://doi.org/10.4067/S0718-221X2023000100415.
[88] S.R. Kadam, V.R. Mate, R.P. Panmand, L.K. Nikam, M.V. Kulkarni, R.S. Sonawane, B.B. Kale, A green process for efficient lignin (biomass) degradation and hydrogen production via water splitting using nanostructured C, N, S-doped ZnO under solar light, RSC Adv. 4 (2014), https://doi.org/10.1039/c4ra10760h.
[89] A. Ramos-Corona, R. Rangel, J. Espino, J. Lara, R. Nuñez, P. Bartolo-Pérez, J. J. Alvarado-Gil, High-yield of Lignin degradation under N-ZnO/Graphene oxide compounds, Catal. Today (2022) 392–393, https://doi.org/10.1016/j.cattod.2021.04.022.
[90] S. Kausar, A. Ali Altaf, M. Hamayun, M. Danish, M. Zubair, S. Naz, S. Muhammad, M. Zaheer, S. Ullah, A. Badshah, Soft template-based bismuth doped zinc oxide nanocomposites for photocatalytic depolymerization of lignin, Inorganica Chim. Acta 502 (2020), https://doi.org/10.1016/j.ica.2019.119390.
[91] S. Malato, P. Fernández-Ibáñez, M.I. Maldonado, I. Oller, Solar photocatalytic processes: water decontamination and disinfection, New Future Dev. Catal. Solar Photocatal. (2013) 371–393, https://doi.org/10.1016/B978-0-444-53872-7.00017-0.
[92] X. Kang, S. Liu, Z. Dai, Y. He, X. Song, Z. Tan, Titanium dioxide: from engineering to applications, Catalysts. 9 (2019), https://doi.org/10.3390/catal9020191.
[93] Z. Pei, X. Liu, J. Chen, H. Wang, H. Li, Research Progress on lignin depolymerization strategies: a review, Polymers (Basel) 16 (2024) 2388, https://doi.org/10.3390/POLYM16172388.
[94] H. Chen, K. Wan, F. Zheng, Z. Zhang, Y. Zhang, D. Long, Mechanism insight into photocatalytic conversion of lignin for valuable chemicals and fuels production: a state-of-the-art review, Renew. Sustain. Energy Rev. 147 (2021) 111217, https://doi.org/10.1016/J.RSER.2021.111217.
[95] S. Rehman, R. Ullah, A.M. Butt, N.D. Gohar, Strategies of making TiO2 and ZnO visible light active, J. Hazard. Mater. 170 (2009) 560–569, https://doi.org/10.1016/j.jhazmat.2009.05.064.
[96] F. Jiang, J. Gao, D. Lang, Photocatalytic selective degradation of catechol and resorcinol on the TiO2 with exposed {001} facets: roles of two types of hydroxyl radicals, Catalysts. 12 (2022) 1–10, https://doi.org/10.3390/catal12040378.
[97] C. Minero, G. Mariella, V. Maurino, D. Vione, E. Pelizzetti, Photocatalytic transformation of organic compounds in the presence of inorganic ions. 2. Competitive reactions of phenol and alcohols on a titanium dioxide-fluoride system, Langmuir 16 (2000), https://doi.org/10.1021/la0005863.
[98] F. Jiang, J. Gao, D. Lang, Photocatalytic selective degradation of catechol and resorcinol on the TiO2 with exposed {001} facets: roles of two types of hydroxyl radicals, Catalysts 12 (2022), https://doi.org/10.3390/catal12040378.
[99] U. Mushtaq, J. Park, A. Riaz, V. Ranaware, M.K. Khan, D. Verma, J. Kim, High-Yield production of deoxygenated monomers from kraft lignin over ZnO-Co/N-CNTs in water, ACS Sustain. Chem. Eng. 9 (2021) 3232–3245, https://doi.org/10.1021/ACSSUSCHEMENG.0C08664/SUPPL_FILE/SC0C08664_SI_001.PDF.
[100] B. Zhang, S.-N. Guo, L.-X. Yun, T.-B. Chen, Y.-H. Gu, H.-T. Zhang, C.-G. Hu, J. Wang, Transparent aqueous dispersions of ultrasmall Zno nanoparticles with enhanced oxygen vacancy as efficient pseudohomogeneous photocatalysts for the depolymerization of lignin, (2024). https://doi.org/10.2139/SSRN.4955557.
[101] J. Xu, M. Li, L. Yang, J. Qiu, Q. Chen, X. Zhang, Y. Feng, J. Yao, Synergy of Ni dopant and oxygen vacancies in ZnO for efficient photocatalytic depolymerization of sodium lignosulfonate, Chem. Eng. J. 394 (2020) 125050, https://doi.org/10.1016/J.CEJ.2020.125050.
[102] I.O. Ali, H. Nady, M.I. Mohamed, T.M. Salama, Fabrication and characterization of ZnO and Ag/ZnO nanoparticles for efficient degradation of crystal violet dye in aqueous solution, J. Indian Chem. Soc. 101 (2024) 101480, https://doi.org/10.1016/J.JICS.2024.101480.
[103] M. Lal, P. Sharma, L. Singh, C. Ram, Photocatalytic degradation of hazardous Rhodamine B dye using sol-gel mediated ultrasonic hydrothermal synthesized of ZnO nanoparticles, Results. Eng. 17 (2023) 100890, https://doi.org/10.1016/J.RINENG.2023.100890.
[104] L. Muschallik, C.R. Kipp, I. Recker, J. Bongaerts, M. Pohl, M. Gellissen, M. J. Schöning, T. Selmer, P. Siegert, Synthesis of α-hydroxy ketones and vicinal diols with the Bacillus licheniformis DSM 13T butane-2,3-diol dehydrogenase, J. Biotechnol. 324 (2020), https://doi.org/10.1016/j.jbiotec.2020.09.016.
[105] Budayatin, J. Waluyo, D. Wahyuni, Dafik, Antibacterial effects of Pheretima javanica extract and bioactive chemical analysis using Gas Chromatography Mass Spectrum, J. Phys. Conf. Ser. (2021), https://doi.org/10.1088/1742-6596/1751/1/012055.
[106] T. Tagami, T. Doi, A. Takeda, A. Asada, K. Kiyota, Y. Sawabe, Detection of pyrovalerone as a possible synthetic by-product of 4′-methyl-α-pyrrolidinohexanophenone and 4-methyl-α-ethylaminopentiophenone in illicit drug products, Forensic Toxicol. (2018) 36, https://doi.org/10.1007/s11419-018-0407-z.